Multimodal pipeline for HCP-compatible processing and registration of legacy datasets (MRI, MEG, and EEG)

Ariosky Areces-Gonzalez[1,2*], Deirel Paz-Linares[1,3*], Usama Riaz[1], Min Li[1], Ying Wang[1], Michael Y. Kpiebaareh[1], Maria L. Bringas-Vega[1,3], Jorge Bosch-Bayard[1,4] and Pedro A. Valdés-Sosa[1,3#]

[1]The Clinical Hospital of Chengdu Brain Science Institute, MOE Key Lab for Neuroinformation, School of Life Sciences and Technology, University of Electronic Science and Technology of China, Chengdu, China
[2]Faculty of Technical Sciences, University of Pinar del Río "Hermanos Saiz Montes de Oca", Pinar del Rio, Cuba
[3]Neuroinformatics Department, Cuban Neuroscience Center, Havana, Cuba
[4]McGill Centre for Integrative Neurosciences MCIN, Ludmer Centre for Mental Health, Montreal Neurological Institute, McGill University, Montreal, Canada

*** Contributed equally:**
Ariosky Areces-Gonzalez and Deirel Paz-Linares

 # Correspondence:
Pedro A. Valdes-Sosa
pedro.valdes@neuroinformatics-collaboratory.org

Keywords: computational neuroscience, structural magnetic resonance imaging, electrophysiological source imaging and connectivity, human connectome project

Abstract

Extracting cortical features, which are the most relevant at characterizing structure and function for normal or abnormal brain conditions, would greatly benefit from multimodal neuroimage processing following the surface-based style. This style recognizes the natural definition space for such features due to the layered (surface-based) Cortex structural and functional organization. It may therefore be more sensitive and specific than the former volume-based style. The Human Connectome Project (HCP) multimodal pipelines render high-quality surface-based processing for some of the most consistently acquired neuroimaging modalities, with the quality too reliant on their precise acquisition requirements. Relevant international brain initiatives are espoused to develop an HCP-compatible neuroinformatic facility for the quality-ensured processing of international neuroimaging datasets, which may not follow the specific HCP acquisition requirements, also coined as legacy datasets. We appointed some initiatives to introduce multimodal pipelines in two HCP-compatible processing branches. a) Structural: forward-modeling with geometry (sources and head) and Lead Fields defined for legacy MEG, or EEG, in the HCP individual cortical space (Cifti) obtained from legacy MRI. Our pipeline (Ciftify-MEEG) leverages a more diverse neuroinformatic repository than the HCP structural or MEG pipelines. Ciftify-MEEG produces substantial processing illustrated here with EEG examples, incorporating alternative processing paths and corrections based on a quality control loop and upon qualitative and quantitative indicators. b)

Functional: identifying spectral topographies and connectomes for the cortical oscillatory activity observed in the MEG or EEG frequency bands. We leverage a novel repository of Bayesian sparse inverse methods that target identifying the topographies and connectomes with actual statistical guarantees, the brain connectivity Variable Resolution Electromagnetic Tomographic Analysis (BC-VARETA). Our pipeline design for BC-VARETA, which we denominate Ciftify-bcVARETA, is integrated into the Ciftify-MEEG outputs and with Bayesian sparse priors structured upon Cifti space information. Ciftify-bcVARETA identification is less biased to forward models and more biased to the observations than the HCP pipeline illustrated here with topographies obtained for MEG and EEG legacy databases.

1 Introduction

Electrophysiological source imaging (ESI) has been effectively employed in many brain imaging applications to estimate the underlying brain networks and dynamic brain processes over the years. EEG and MEG have become two main methods for the noninvasive assessment of brain electrical activity, providing unsurpassed temporal resolution in neuroscience research and clinical applications (He, Ding and Sohrabpour, 2020).

One of the significant challenges that introduce ESI research is the moderate spatial resolution of the estimated ESI solutions. Previous studies have indicated that the EEG/MEG source imaging problem can be solved with reasonable resolution and accuracy by incorporating various a priori information, such as anatomic constraints on the sources provided by other imaging modalities like structural MRI (sMRI) or functional MRI (fMRI), where the forward modeling process is essential for the inverse modeling its electro-physical brain origin or source activity (Hämäläinen and Ilmoniemi, 1994). ESI problem being an under-determined optimization problem, a higher spatial resolution is needed. Precisely, conventional algorithms such as, Extract low-resolution brain electromagnetic tomography eLORETA (Pascual-Marqui *et al.*, 2006) and Linear constrainer minimum variance LCMV (Lin *et al.*, 2008) achieve robust inverse imaging at the expense of imposing overly smooth distributions in the source space. Novel inverse solution methods, like Spectral-Structured-Sparse-Bayesian-Learning ssSBL(Paz-Linares *et al.*, 2023) and Hidden Gaussian Graphical Spectral model HiGGS aim at an ESI of the source cross-spectrum controlling common distortions of the estimates and facing a severely ill-conditioned and high-dimensional inverse problem.

Computing ESI to the massive collection of raw data acquired with diverse formats and standards, or preprocessed data following the diverse processing styles, is harvested due to intense clinical or basic neurosciences practice based upon some types of neuroimages; and this is causing a significant gap in quality standards across datasets. Developing a standard neuroinformatic facility for this purpose has been appointed by relevant international initiatives and bridge this gap. Some of these initiatives are the Global Brain Consortium (GBC), Helmholtz International BigBrain Analytics and Learning Laboratory (HIBALL), Healthy Brain Networks (HBN), and Cuba Canada China Axis (CCC-AXIS).

A standard neuroinformatic facility through processing pipelines that may perform strongly for most datasets, such as that appointed by these initiatives, is concealed by three fundamental guidelines:

1) Concurrent and standardized processing of multimodal neuroimaging, structural and functional, across large and diverse human or animal datasets.
2) Mapping multimodal imaging onto a structural template space that is homeomorph to all human brains.

3) Characterizing brain states by modeling and estimating the multidimensional (structural and functional) neural features from multimodal imaging.

These initiatives have been espoused to a conception of neuroinformatic facilities inspired by the design of processing pipelines developed by the WU-Minn consortium: Human Connectome Project (HCP)(Van Essen *et al.*, 2013). The HCP consortium introduced the minimal pipelines standardizing the processing for some of the most consistently acquired neuroimaging modalities, such as structural MRI (sMRI), functional MRI (fMRI) (Glasser *et al.*, 2013), diffusion MRI (dMRI) (Sotiropoulos *et al.*, 2013), and Magnetoencephalogram (MEG) (Larson-Prior *et al.*, 2013). A specific justification has been introduced by the HCP pipelines, which base 1), 2), and 3) upon cortex-specific multimodal (structural and functional) features and Surface-based processing of multimodal imaging.

Achieving precision in the inverse modeling of source activity, which is currently at stake (He *et al.*, 2019; Reid *et al.*, 2019), cannot underestimate the detail and realism of the forward model (Akalin Acar and Makeig, 2013). This is a critical condition due to an unstable, multivariate, and nonlinear effect of the forward model even for the simplest inverse model (Pascual-Marqui, Michel and Lehmann, 1994; Trujillo-Barreto, Aubert-Vázquez and Valdés-Sosa, 2004; Mattout *et al.*, 2006; Pascual-Marqui *et al.*, 2006; Friston *et al.*, 2008; Paz-Linares *et al.*, 2017).

Precise modeling (inverse or forward) would depend on the Lead-Field obtained for highly detailed anisotropic 3D models of the geometry and electromagnetic properties of biological tissue (head) and each human individual (valid also for other animals) (Nolte and Dassios, 2005; Hallez *et al.*, 2007; Dannhauer *et al.*, 2011, 2012; Windhoff, Opitz and Thielscher, 2013; Vorwerk *et al.*, 2014, 2018; Yamaguchi, 2014; Piastra *et al.*, 2020). Such a level of detail is also encompassed by a huge cost and would be impractical in large datasets, employing the Finite Element Method (FEM) computations (Strang, Fix and Griffin, 1974). It is common in neuroimaging to assume isotropic and piecewise homogeneous electromagnetic properties of biological tissue, which bypasses such cost and preserves a moderate level of detail in Lead-Field computations. Even moderately detailed forward modeling must deal with the electric field potentials under conductivity heterogeneities at tissue boundaries (Hämäläinen *et al.*, 1993; Riera and Fuentes, 1998), and complex numerical computations via the Boundary Elements Method (BEM) (Cheng and Cheng, 2005).

Structural Magnetic Resonance Imaging (sMRI) has prevailed as the most established technique for segmenting brain tissue in vivo (Jackson *et al.*, 1997). Legacy processing tools –defined before the Human Connectome Project (HCP) pipelines —such as Freesurfer (Fischl, 2012) allow the extraction from T1 sMRI images of different brain structures, such as the cortical layers and subcortical structures, e.g., the thalamus. T1 refers to the sMRI image that captures the different tissue-specific relaxation times for the magnetic fields induced in the transverse plane –to MRI B0 field— during gradient echo or spin echo MRI sequences (Bonaiuto *et al.*, 2018). The B0 field is the permanent magnetic field of the MRI equipment used to induce the precession of the nuclear spin of hydrogen atoms. Freesurfer also allows studying different brain structures or features based on T2-weighted images. These images are a type of sMRI image obtained by the contrast derived from different relaxation times in the direction of the B0 field.

Cortical structural and functional features are the most relevant at characterizing all advanced brain functions and are, therefore, the target of the most consistently acquired imaging modalities. A reductionism for brain state characterization hinges on cortical neuroelectric processes that are driven

by structural and functional features, such as cortex structural and functional connectivity (Uddin, 2013), layer-specific connectivity and dynamics in the Cortex (Vinck and Perrenoud, 2019), and atlases of the cortical structural and functional organization (Glasser *et al.*, 2016). Noninvasive imaging modalities may allow invivo characterization of features that drive the mean field neuroelectric dynamic produced by thousands of neurons (Valdes *et al.*, 1999) in layers of the elementary logical unit denominated cortical hypercolumn (Buxhoeveden and Casanova, 2002).

Surface-based functional imaging processing based on the cortical structural space increases the accuracy in extracting cortex-specific neural features. The type of pipelines that can extract with much more accuracy cortical features makes use of surface-based processing instead of volume-based processing for structural (Coalson, Van Essen and Glasser, 2018) or functional (Anticevic *et al.*, 2008) imaging. Accepting the layered cortical organization (surface-based) processing may be more specific and sensitive to the actual physiological activity that resides in a superficial structural space (Dale, Fischl and Sereno, 1999). This would produce a higher quality in cortical maps for features obtained from the indirect observation of neural activity in signals produced via metabolic-hemodynamic (Brodoehl *et al.*, 2020) or electrical (Nunez *et al.*, 1994; Grech *et al.*, 2008) mechanisms.

The HCP structural pipeline (Glasser *et al.*, 2013; Van Essen *et al.*, 2013), which is designed to extract the segmentation based on both T1 and T2 sMRI, uses Freesurfer for an intermediate step in a processing pipeline that includes preeFreesurfer (registration of T1 and T2) and postFreesurfer (construction of volumetric and superficial canonical spaces based on FSAverage template). The HCP pipelines leverage a new type of format (Cifti), which was preceded by Nifti (Jenkinson, 2005) and Gifti (Harwell, J., Bremen, H., Coulon, O., Dierker, D., Reynolds, R.C., Silva, C., Teich, K., Van Essen, D.C., Warfield, S.K. and Saad, 2008), originated due to the need of improving the efficiency in the intensive processing of cortically mapped MRI data. The Cifti format allows for highly efficient storage and processing with high-quality standards. The combined volumetric (subcortical) and surface (cortical) data produce high-quality registration of functional signals with surface-based processing. An essential ingredient is the new definition of the gray matter physical space: Cifti gray ordinates, the substrate for the surface-based processing style of the HCP. Cifti gray ordinates are the space where all structural and functional features reside in HCP pipelines. These leverage a data structure, combining surfaces to define the cortical layers and volumes to define subcortical structures.

Due to the high-quality acquisition standards met by this type of processing, extensions have been developed for specific purposes using different alternative software packages, such as CIFTIFY (Dickie *et al.*, 2019), which considers the case of legacy databases containing only T1 sMRI to achieve a standard format and registration across all databases. The Ciftify pipeline (Dickie *et al.*, 2019) adopts the HCP style for adapting the HCP preprocessing for legacy datasets. Within this framework, any functional dataset with accompanying anatomical data can be analyzed in CIFTI format. This framework adapts the structural module of the HCP pipelines to datasets that acquire only T1w images but do not include the ESI processing, delegating this process to the same module used in the HCP pipeline in charge of the inverse solution, the "megconnectome" pipeline based on Fieldtrip that analysis the MEG data in the HCP (Larson-Prior *et al.*, 2013) and only dedicated for this specific dataset.

Functional imaging based on MEG and EEG modalities directly reflects mechanisms underpinned by purely neural activity (Piastra *et al.*, 2021). Especially EEG (which was not included in the HCP processing) is the most intensively exploited in brain research and clinical applications (Symms, 2004; Ulbert *et al.*,

2004; Larson-Prior *et al.*, 2013). HCP has included MEG pipelines using Fieldtrip (Oostenveld *et al.*, 2011), linked to geometric files from the structural processing pipeline for T1 and T2 sMRI and the MEG 4D-Neuoroimaging data. Recently the HCP-compatible modeling of brain generator, head volume conduction, and Lead Fields was also proposed through the Brainstorm suit (Tadel *et al.*, 2011).

A fundamental problem with Fieldtrip and Brainstorm pipelines for HCP is that these are limited to producing only MEG head models and Lead Fields and sMRI-based generator models, only from the specific geometric files collected and preprocessed according to the HCP sMRI and MEG standards (Larson-Prior *et al.*, 2013). The head models and Lead Fields a) are explicitly designed for MEG and, therefore, lack the supplementary files with conductivity compartments to define EEG head models and Lead Fields. Another problem is with the registration sensor layout. HCP MEG contains predefined transformation matrices to map the MEG sensors in the sMRI space, which require specific acquisitions adopted within the HCP standards. Such acquisition standards would not apply to MEG or EEG legacy databases. The surface-based source models are extracted using specific resampling methods in the individual space, with common FSAverage topology (geometrical neighbor structure in the gray matter) with a low-resolution discretization (8K). Such source models cannot be redefined directly from the standard HCP structural outputs (Glasser *et al.*, 2013) or CIFTIFY outputs (Dickie *et al.*, 2019).

Other neuroinformatic facilities based on Fieldtrip (Oostenveld *et al.*, 2011) and SPM12 (Henson *et al.*, 2019) describe the steps involved in analyzing multimodal, multi-subject human neuroimaging data. These pipelines are specific to processing the BiDS format dataset that contains electroencephalographic (EEG), magnetoencephalographic (MEG), and functional and structural magnetic resonance imaging (MRI), but not legacy datasets. The user has to develop the processing tools for the analysis of the whole dataset, and these processes do not include our novel method for ESI

Neural electrical activity is linearly propagated and registered with millisecond temporal resolution on MEG/EEG head sensors due to the linear nature electromagnetic forward model (MacKay, 2003; McLachlan and Krishnan, 2007; Lopes da Silva, 2013). It is to be noted that, despite widespread misconceptions, fMRI (considered in HCP acquisitions and pipelines) reflects poorly the neural electrical activity, which is distorted, temporally by nonlinear propagation and spatially by blurring, of the metabolic-hemodynamic forward model (Piastra *et al.*, 2021). Therefore, incorporating MEG/EEG and fMRI would be much more valuable to achieve the goal of the second release for the HCP processing pipelines (Ulbert *et al.*, 2004), which is the precise determination of spectral properties for neural processes or spectral network topographies and topologies with cortical support (Neal, 1998; Nagasaka, Shimoda and Fujii, 2011; Nunez, Nunez and Srinivasan, 2019; Nolte *et al.*, 2020). Electrophysiological Source Imaging (ESI) reflects brain activity with millisecond temporal accuracy and could help avoid temporal aliasing in determining neural causal relations (Avants, Tustison and others, 2014; Vassal *et al.*, 2016). EEG/MEG ESI is affected differently due to their low resolution and blurring effect of head volume conduction-leakage (Das *et al.*, 2012; Sherif *et al.*, 2014; Helbling *et al.*, 2015).

ESIC, based upon the MEG/EEG, would be more accurate using novel methods that acknowledge the most severe difficulty of ESIC: distortions in the topographies and topologies of networks determined from the MEG/EEG due to their limited spatial resolution. Methods to improve ESIC would be based upon the statistical guarantees of Bayesian inference with mathematical sparsity priors. Also, ESIC would be much more accurate if it were computed in the individual subject space and informed with priors, given the structural information from sMRI and structural priors, which in this case shall be consigned to

the Cifty gray ordinates space. This process would provide a group of parameters to describe individual brain dynamics with an excellent temporal resolution. It would therefore provide the means for understanding and validating the various neurophysiological mechanisms and emphasizing different brain states in normal conditions or interpreting the impairment produced by different diseases, which would require informing across individuals such space of parameters that give rise to individual brain dynamics.

Table 1 shows the comparative features of the most useable initiatives for multimodal image processing. Note that we highlight in the table some of their futures based on the target of our research.

Table 1 Comparative features of multimodal pipelines

Features \ Pipelines		HCP pipelines	Ciftify	Fieldtrip	SPM12	CiftiStormESI
Process integration		✗	✗	✗	✓	✓
Legacy acquisition support		✗	✓	✓	✗	✓
EEG analysis		✗	✗	✓	✓	✓
MEG analysis		✓	✗	✓	✓	✓
Cifti format		✓	✓	✓	✗	✓
Structural processing	T1&T2	✓	✗	✗	✗	✓
	T1 alone	✗	✓	✓	✓	✓
	No sMRI	✗	✗	✗	✗	✓
Forward model	OpenMEEG BEM	✗	✗	✓	✓	✓
	Duneuro FEM	✗	✗	✓	✗	✓
	Overlap Spheres	✗	✗	✓	✓	✓
	Single Sphere	✗	✗	✓	✓	✓
eLORETA		✓	✗	✓	✓	✓
LCMV		✓	✗	✓	✓	✓
Activation ESI (sSSBL)		✗	✗	✗	✗	✓
Connectivity ESI (HiGGS)		✗	✗	✗	✗	✓

2 Materials and Methods

2.1 Ciftify-MEEG pipeline: Surface-based structural processing and modeling MEG/EEG sources, head, and Lead Fields with HCP compatibility through using a diverse neuroinformatics ecosystem.

The HCP-compatible MEG and EEG source processing pipeline (Ciftify-MEEG) are based on HCP-like structural MRI (sMRI) processing and Brainstorm MEG/EEG source/head modeling; we achieve quality-ensured computation of the Lead Field for EEG and MEG. The sMRI processing for the obtention is based on the HCP structural pipeline for cases that include T1 and T2 MRIs, the CIFTIFY pipeline for datasets that include only T1 MRIs, and Brainstorm structural template for those does not have T1 or T2 MRI images. See Figure 1 left shows the specific processing in each situation to obtain the structural segmentations like HCP standards. Code with batch processors that produces the geometrical structures and Lead Field, which invokes the HCP structural pipeline, CIFTIFY, and source/head modeler based on FSL and the Brainstorm suit is freely available in GitHub:

https://github.com/CCC-members/HCP_compliant_processor

https://github.com/CCC-members/HCP_BST_source_head_modeler

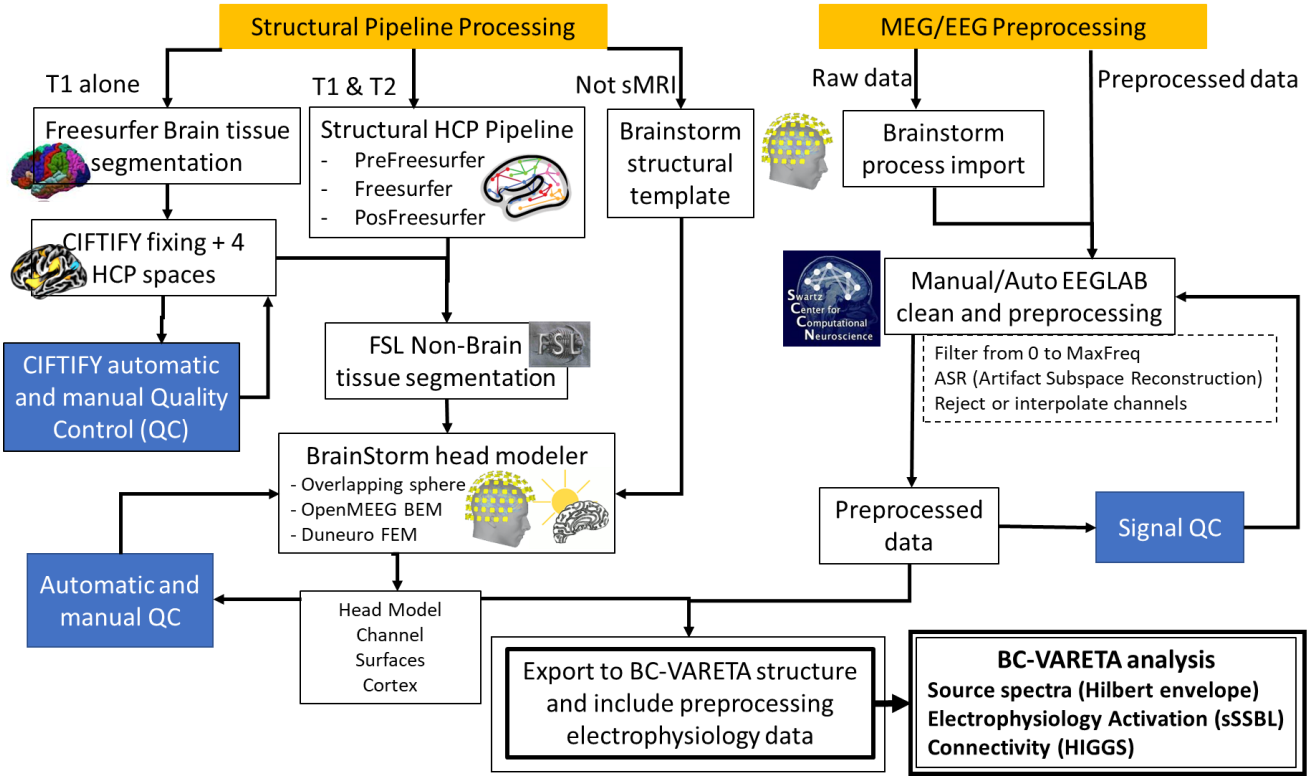

Figure 1 General diagram for the HCP-compliant pipeline processing.

The HCP structural pipelines produce T1/T2 MRI or T1 MRI images registered linearly to the MNI space, and the corresponding gray matter volumetric and superficial spaces, obtained from a segmentation of brain tissue based on the nonlinear registration of T1/T2 MRI or T1 MRI images onto the FSAverage template. The volumetric and superficial spaces are in one-to-one correspondence to the FSAverage volumetric and low-resolution (64K and 32K) canonical spaces. They, therefore, allow rapid mapping of the structural or functional information (given in volume or surface) onto FSAverage space, which is used then to compare the results obtained in the analysis of brain activity and connectivity across databases. In Figure 2, we illustrate this anatomical substrate of HCP-compliant pipelines, which provides structural outputs for T1/T2 MRI or T1 MRI images.

Top row: a) Structural MRI pipeline outputs based obtained from Freesurfer and Ciftify processing for MRI T1 images (legacy databases) and b) HCP preFreesurfer, Freesurfer and postFreesurfer processing for MRI T1 and T2 images (HCP like databases). c) HCP structural spaces (volumetric and superficial) in the individual and FSAverage (MNInonlinear) spaces at 32K resolution. Bottom row: Other HCP structural outputs used to implement priors for the surface-based analysis of brain activity and connectivity or modeling: d) cortical curvature, e) thickness, f) parcellation, g) volumetric subcortical segmentation, and h) cortical layers mid-thickness and pial.

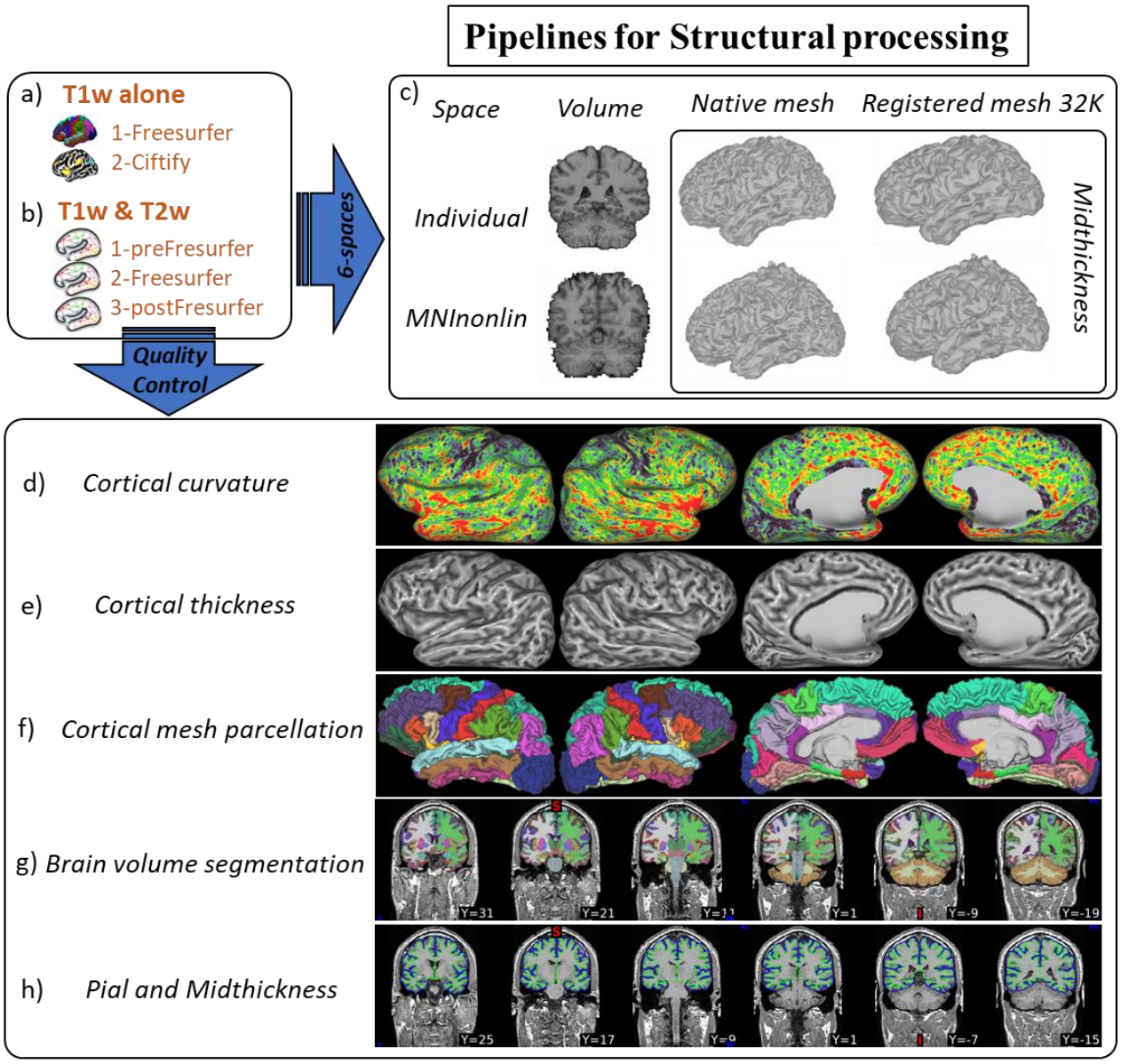

Figure 2 Structural processing with Ciftify and HCP Pipeline

We developed a pipeline for the computation of the MEG/EEG Lead Field with HCP-like structural outputs based on modular and low-level programming using Brainstorm (BST) functionalities. A type of pipeline that processes specific HCP source and head model outputs, obtained through Fieldtrip (Oostenveld *et al.*, 2011), has been proposed by the Brainstorm team (Tadel *et al.*, 2011) to process the HCP MEG database.

In Figure 3, we illustrate some steps of our pipeline that have been proven vital in the analysis, even for databases of extremely poor-quality standards. We perform the registration of sensors for MEG and EEG using: a) the SPM canonical surface envelope of the actual scalp (the first row left). b) The actual scalp was obtained by means of FSL, along with the inner skull and outer skull used as conductivity layers for the computation of the EEG Lead Field. The T1 MRI and cortical surfaces are the native HCP outputs registered linearly to the MNI space. c) In the second row, see the correct registration of the HCP cortical surface and the three FSL conductivity layers (inner skull, outer skull, and scalp). The registration of d) EEG electrodes and e) MEG gradiometers are shown in the third and fourth rows of the figure. The Lead Fields are computed using f) MEEG Overlapping Spheres (BST code) for MEG (Huang, Mosher and Leahy, 1999) and g) Open MEEG for EEG (Theaud et al., 2020). See plots of the estimated Lead Fields for a given reference sensor, in the fifth row for a MEG gradiometer and in the sixth row for an EEG electrode.

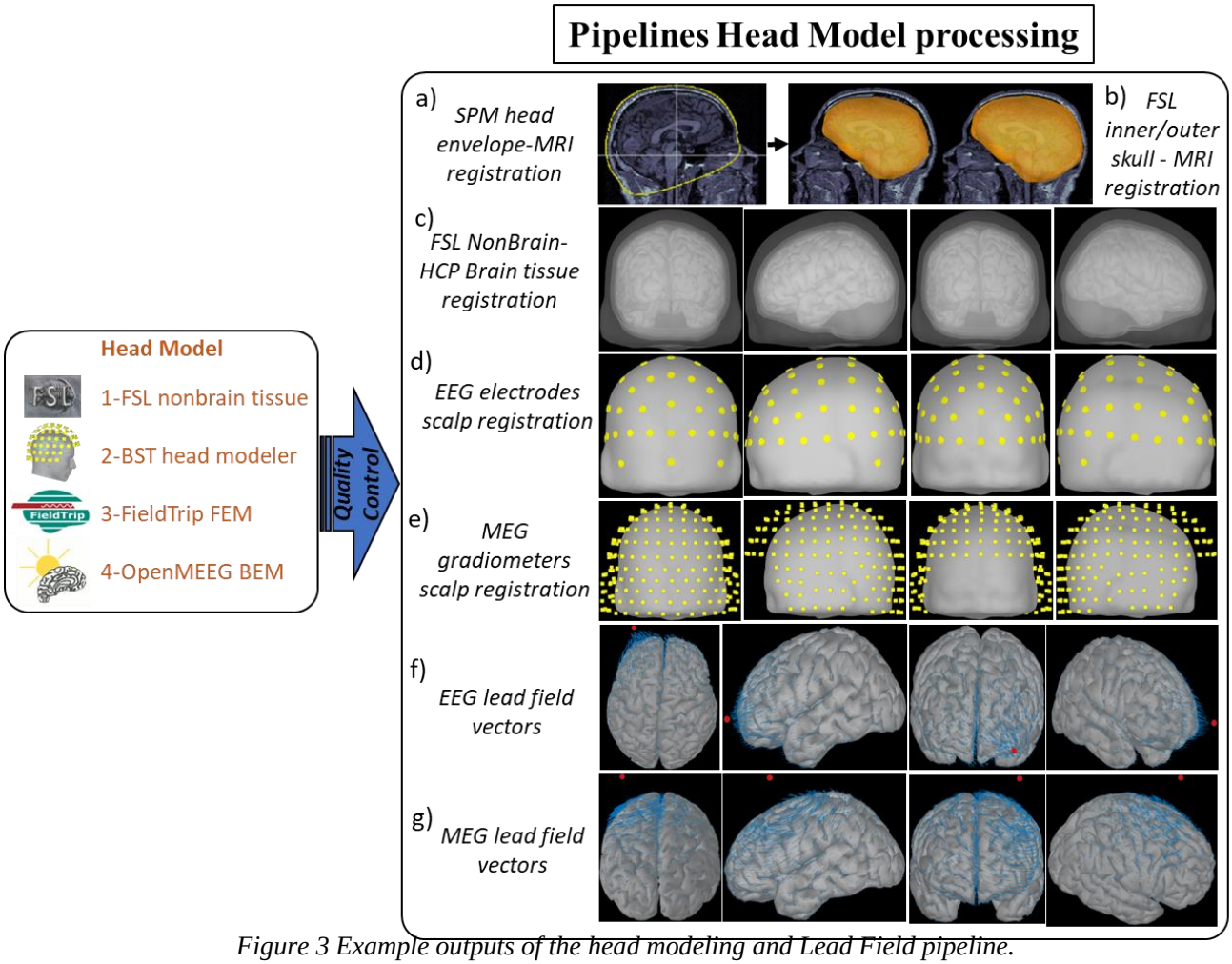

Figure 3 Example outputs of the head modeling and Lead Field pipeline.

A loop for the rejection or correction of cases was implemented as the final stage of the structural and head modeling pipeline. In Table 2, we have summarized with figures 1-16 the indicators for the quality control (QC) report for a case selected from the CHBMP database. We control three leading indicators:

Step 1) Segmentation of cortical and nonbrain tissue (inner-skull, outer-skull, and scalp); see figures 1-6 in Table 2.

Step 2) MEG/EEG sensor registration. See figures 7-8 in Table 2.

Step 3) MEG/EEG Lead Field, see figures 9-16 in Table 2.

Based on the visual inspection of the quality control (QC) indicators mentioned above, we can either reject the case or recompute the head model and Lead Field:

Correction 1) By substituting the individual subject HCP structural outputs and FSL nonbrain tissue by chosen template outputs, which can be used to perform approximated electrophysiological source imaging from the MEG/EEG. To facilitate this process, a specific parameter in the pipeline configuration files allows individualized switching or a predetermined template anatomy. We make the default HCP and FSL structural outputs available for the ICBM, FSAverage, and Collins templates.

Correction 2) By modifications to the sensor layout. To this end, the pipeline output files are loaded by calling on the BST graphical interface, corrected manually, saved, and flagged. Then, when the pipeline is called in batch mode, the flagged files are post-processed by the module dedicated to Lead Field computation alone.

In Figure 4, we show an example of a case that was rejected due to the following:

2.1) Movement and noise artifacts of the MRI (top left) that have consequences in the topology of the segmentation (bottom left).

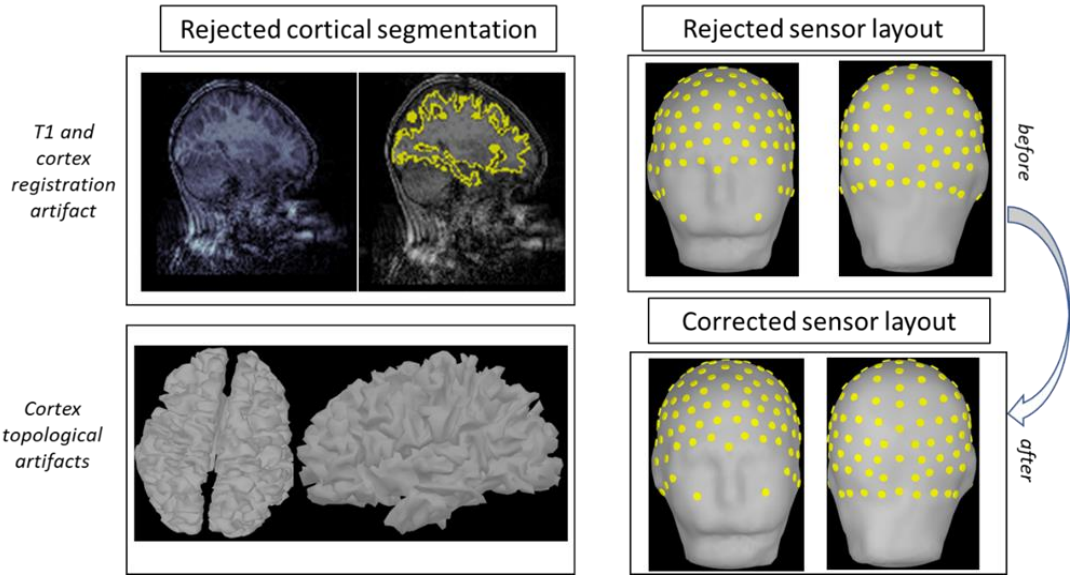

Figure 4 Case example for the quality control of cortical segmentation and sensor-scalp registration

2.2) Wrong scalp registration of the EEG sensors (top right) that was corrected manually (bottom right).

2.2 Ciftify-bcVARETA pipeline: Spatially resolved MEG/EEG source spectral networks mapping with HCP compatibility using sparse and surface-based structural priors.

We incorporate novel methods designed to minimize the distortions of specific statistical quantities to be estimated by directly introducing mathematical priors (Paz-Linares *et al.*, 2018; Gonzalez-Moreira *et al.*, 2020). This style contrast with the conventional two-step approach used by HCP pipelines:

Step 1) Estimation of the time series of source activity.

Step 2) Determination of statistical quantities, such as the second-order statistical moment of the Fourier transform (Spectrum) and its covariance (Cross-spectrum).

Instead of a two-step approach, BC-VARETA uses Bayesian evidence to determine 2) from the MEG/EEG data, which provides proper statistical guarantees. An essential ingredient for such statistical guarantees is the mathematical sparsity priors used by BC-VARETA to estimate the source spectrum via Spectral Structured Sparse Bayesian Learning (sSSBL) (Gonzalez-Moreira *et al.*, 2020; Paz-Linares *et al.*, 2023) and the cross-spectrum or connectivities via the Hidden Gaussian Graphical State (HIGSS) model (Paz-Linares *et al.*, 2018). We also incorporate in this toolbox conventional two-step approaches based on methods for the estimation of activity, such as exact Low-Resolution Tomographic Analysis (eLORETA) (Pascual-Marqui *et al.*, 2006) and Linearly Constrained Minimum Variance (LCMV) (Van Veen *et al.*, 1997). These have been optimally implemented for the type of analysis in the spectral domain to estimate spectral and cross-spectra. BC-VARETA also incorporates priors based on HCP anatomy to provide the spectra and cross-spectra with structured sparsity.

Code with batch processors for BC-VARETA freely available in GitHub:

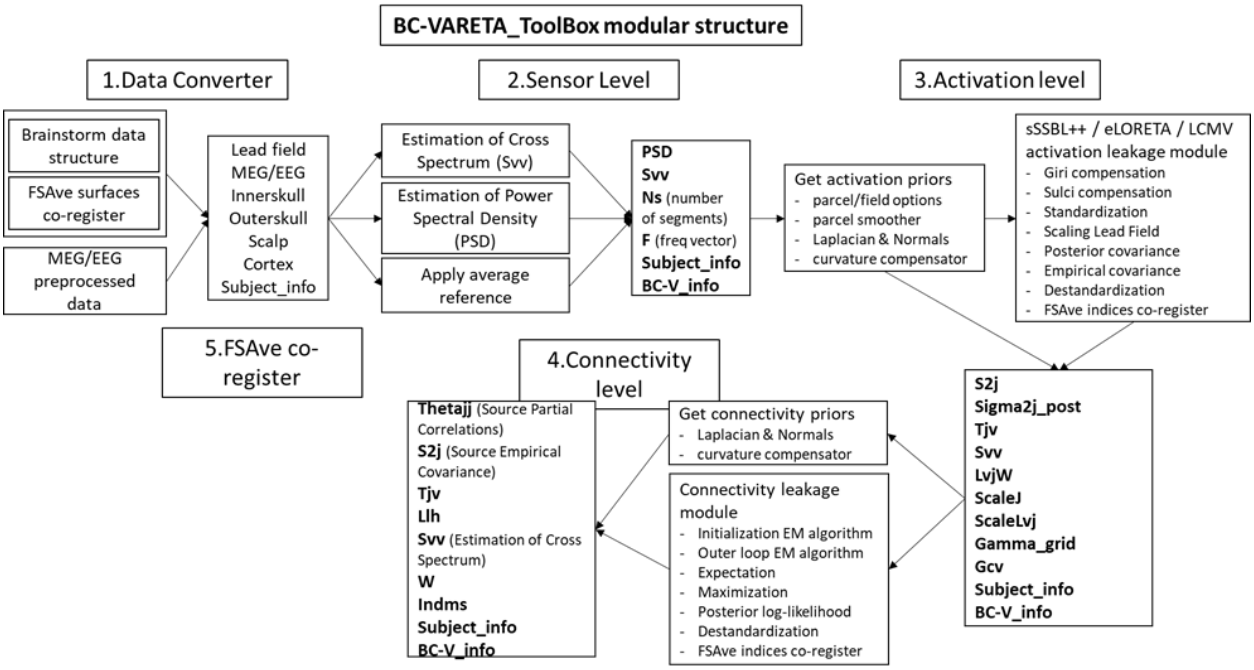

Figure 5 Modular structure of BC-VARETA Toolbox.

https://github.com/CCC-members/BC-VARETA_Toolbox

BC-VARETA was programmed in five modules that we illustrate in Figure 5 in a hierarchical order. In Figure 6, we describe the outputs of BC-VARETA, given by modules: 2 (sensor level analysis) using the Hilbert envelope of the filtered data and Slepian windows, 3 (activation level analysis) using the spectral Structured Sparse Bayesian Learning (sSSBL) method (Gonzalez-Moreira *et al.*, 2020; Paz-Linares *et al.*, 2023) and 4 (connectivity level analysis) the Hidden Gaussian Graphical State-Model (HIGGS) with connectivity regularization of the Hermitian Graphical LASSO (hgLASSO) method (Paz-Linares *et al.*, 2018).

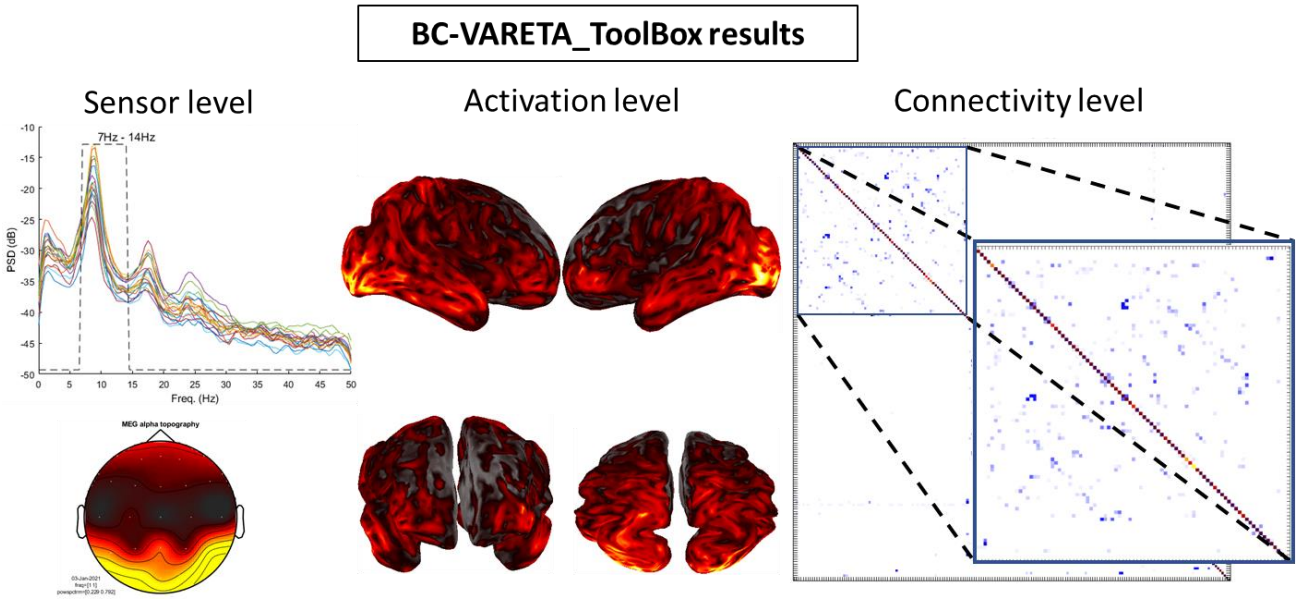

Figure 6 BC-VARETA outputs for the alpha band with one of our methods

Module 1) Converter for files from HCP structural and head modeling pipeline and MEG/EEG data to be loaded in BC-VARETA analysis.

Module 2) Sensor level analysis via the FFT of the MEG/EEG signals to produce the cross-spectra and the spectra and specific band topographies for quality control.

Module 3) Activation level analysis via sSSBL spectral electrophysiological source imaging to obtain the MEG/EEG source spectra.

Module 4) Connectivity level analysis via HIGGS spectral electrophysiological source connectivity.

Module 5) Registration to common structural space via interpolating the low-resolution cortex discretization to the individual subject.

Using the methods sSSBL for 3 (activation level) and HIGGS/hgLASSO for 4 (connectivity level), which we illustrated in Figure 5, is the optimal setup for BC-VARETA toolbox since these provide statistical guarantees, which we explain here briefly. An unbiased level of sparsity was obtained for sSSBL with the F-score computed from the rate between the explained variances $\hat{\boldsymbol{s}}_{\boldsymbol{\iota}}^2(\nu)$ and residual variances $\breve{\boldsymbol{\sigma}}_{\boldsymbol{\iota}}^2(\nu)$ of the posterior distribution $N^{\mathcal{C}}\left(\boldsymbol{\iota}_m(\nu)\middle|\hat{\boldsymbol{\iota}}_m(\nu),\breve{\boldsymbol{\Sigma}}_{\boldsymbol{\iota}\boldsymbol{\iota}}(\nu)\right)$ for the mixed effect model of the proper sources (Gonzalez-Moreira *et al.*, 2020):

$$\boldsymbol{\iota}_m(\nu) = \hat{\boldsymbol{\iota}}_m(\nu) + \boldsymbol{\zeta}_m(\nu) \tag{1}$$

Where the explained variances are computed as $\hat{\mathbf{s}}_{\boldsymbol{\iota}}^2(\nu) = diag(\hat{\mathbf{S}}_{\boldsymbol{u}}(\nu))$ with $\hat{\mathbf{S}}_{\boldsymbol{u}}(\nu) = (1/\mathrm{m})\sum_{i=1}^{\mathrm{m}} \hat{\boldsymbol{\iota}}_m(\nu)\hat{\boldsymbol{\iota}}_m^{\dagger}$, the residual variances $\breve{\boldsymbol{\sigma}}_{\boldsymbol{\iota}}^2(\nu) = diag(\breve{\boldsymbol{\Sigma}}_{\boldsymbol{u}}(\nu))$ with $\breve{\boldsymbol{\Sigma}}_{\boldsymbol{u}}(\nu)$ the estimator of the posterior covariance. The F-score is $F = \hat{\mathbf{s}}_{\boldsymbol{\iota}}^2(\nu)/\breve{\boldsymbol{\sigma}}_{\boldsymbol{\iota}}^2(\nu) > 1$, which tests the hypothesis that the fixed effect $\hat{\boldsymbol{\iota}}_m(\nu)$ is larger than the residuals $\boldsymbol{\zeta}_m(\nu)$.

HIGGS produces an unbiased estimation of the connectivity. In the first place, it eliminates the bias of $\boldsymbol{\Theta}_{\boldsymbol{u}}(\nu)$ via "de-sparsification":

$$\left(\widehat{\boldsymbol{\Theta}}_{\boldsymbol{u}}^{(k+1)}(\nu)\right)_{unb} \leftarrow 2\widehat{\boldsymbol{\Theta}}_{\boldsymbol{u}}^{(k+1)}(\nu) - \widehat{\boldsymbol{\Theta}}_{\boldsymbol{u}}^{(k+1)}(\nu)\breve{\boldsymbol{\Psi}}_{\boldsymbol{u}}^{(k)}(\nu)\widehat{\boldsymbol{\Theta}}_{\boldsymbol{u}}^{(k+1)}(\nu) \tag{2}$$

This is an extrapolation to the complex domain of the unbiased estimator for the Graphical LASSO theory of Jankova and Van De Geer. Debiasing $\boldsymbol{\Theta}_{\boldsymbol{u}}(\nu)$ is particularly relevant to produce reliable neural connectivity estimates that depend on it. This debiased estimator has an additional advantage, allowing us to carry thresholding of the connectivity to obtain reliable sparse estimators.

As it is shown in (Paz-Linares *et al.*, 2018), the unbiased estimator for HIGGS $\left(\widehat{\boldsymbol{\Theta}}_{\boldsymbol{u}}^{(k+1)}(\nu)\right)$ follows the distribution:

$$\left(\widehat{\Theta}_{\boldsymbol{u}}^{(k+1)}(\nu;i,j)\right)_{unb} \sim N_1^{\mathbb{C}}\left(\left(\widehat{\Theta}_{\boldsymbol{u}}^{(k+1)}(\nu;i,j)\right)_{unb} \middle| \Theta_{\boldsymbol{u}}(\nu;i,j), \frac{\sigma_{ij}}{\sqrt{\mathrm{m}}}\right) \tag{3}$$

$$\sigma_{ij} = \widehat{\Theta}_{\boldsymbol{u}}^{(k+1)}(\nu;i,i)\widehat{\Theta}_{\boldsymbol{u}}^{(k+1)}(\nu;j,j) + \widehat{\Theta}_{\boldsymbol{u}}^{(k+1)}(\nu;i,j) \tag{4}$$

with a fixed value of the regularization parameter $\alpha_{\boldsymbol{\iota}} = \sqrt{\mathrm{m}\, log(\mathrm{q})}$ and m "q, whose z-statistic possesses a Rayleigh distribution with variance $1/\sqrt{2}$.

$$z(\nu;i,j) \sim 2e^{-z^2(\nu;i,j)} z(\nu;i,j) \tag{5}$$

$$z(\nu;i,j) = \sqrt{\left|\sqrt{\mathrm{m}}\left(\widehat{\Theta}_{\boldsymbol{u}}^{(k+1)}(\nu;i,j)\right)_{unb} / \sigma_{ij}\right|} \tag{6}$$

The values of $\widehat{\Theta}_{\boldsymbol{u}}^{(k+1)}(\nu)$ with $z(\nu;i,j)$ is lower than a threshold z-scored to ensure a Family Wise Error of type I. It is to be noted that this debiasing and thresholding yields, in the final iteration, a statistically guaranteed thresholded connectivity matrix.

The analysis in 2 (activation level) and 3 (connectivity level) can also be carried out in multiple combinations of physical priors, which can be evoked for all methods. These are included in JSON configuration files, along with general configuration and other control parameters depicted in Figure 6. The physical priors refer to parameters organized in two groups: 1) spectral constraints and 2) gray matter structural constraints.

There are four modes of constraints based on the following assumptions for activations or connectivities concerning different frequencies in the spectra: 1) activations or connectivities are independent for every frequency component. This is the mode run by frequency bin = 1 (for the logical parameter in Figure 6a), which is very consuming in terms of time and memory 2) activations or connectivities are common for every frequency band. This mode, run by frequency bin = 0 (for the logical parameter in Figure 6a) using the average cross-spectra of every frequency band (that are defined in Figure 6b), is

more economical in terms of time and memory, as well as increase the sample number by a factor equal to the number frequency bins in the band. 3- the spatial support of the activations and connectivity (nonzero values) is common for all frequencies in the spectra. This is the mode system response = 1 (for the logical parameter in Figure 6a) that uses the average F-scores for all frequencies, which is devoted to the post-processing of the connectivity tensor via spectral factorization analysis to obtain the directed connectivity.

There are four modes for the structural constraints based on assumptions for the gray matter spatial distribution of activations and connectivities (Figure 6c and Figure 6d):

a) The scale of activations or connectivities at every point of the cortical surface in linear proportion to the cortical curvature so that their visibility at the gyri is more significant than at the sulci. This is the mode IsCurv = 1 (Figure 6c), which performs a linear transformation of the Lead Field with optimal slope and intercept (cross-validated in simulations) that are different for the giri (aGiri, bGiri) and sulci (aSulc, bSulc).
b) There is a high likelihood for the activations or connectivities to reinforce each other in closed regions or parcels, given the functional organization of cortical space, this mode IsParcel = 1, which uses sparse group penalization of activity and connectivity of the parcels defined within a cortical atlas.
c) There is a high likelihood of neighbor activations or connectivities reinforcing each other, given the large density of lateral connections in the Cortex. This mode IsNeigh = 1, which performs a matrix transformation of the Lead Field by the inverse Laplacian. We use the deformed graph Laplacian with an optimal regularization parameter regLaplacian (cross-validated in simulations).
d) There is a high likelihood for the activation vector's three components (X, Y, Z) and their connectivity to reinforce each other, given their origin in a common physical magnitude described by a vector field. These can be constrained in three different ways that assume different degrees of strength in their coupling, mode IsField = 1, which carries the fields generally oriented to the cortical surface, IsField = 2 assumes the field probabilities are rotationally invariant to the surface normal, and IsField = 3 that assumes the field probabilities are spherically invariant.

3 Results

3.1 Achieving flexible Ciftify-MEEG processing in large legacy (sMRI, MEG/EEG) datasets using a quality control loop and automatic/manual corrections based on diverse quality indicators and supervised by expert criteria

We have performed the initial test of concept for the structural processing and head modeling in three public datasets: Human Connectome Project (HCP) (Larson-Prior *et al.*, 2013), Cuban Human Brain Mapping (CHBMP) (Valdes-Sosa *et al.*, 2021) and Healthy Brain Network (HBN)(Alexander *et al.*, 2017). The raw and processed data for these databases, amongst others, is being curated in the CCLab high-performance computer (HPC). The same data is mirrored in Compute Canada and will be reflected in Cuba as part of the Collaborative effort carried out by CCLab in the Cuba-China-Canada project. These are part of the set of databases stored in the CCLab high-performance computer, which contain several modalities that we summarize in Table 1, where we have highlighted the databases used for the initial test of concept.

We now emphasize that our objective is to produce the space features based on these multiple modalities, and to facilitate cross-modality comparison, following the high-quality HCP-like processing

and through the registration FSAverage space. Remarkably, the HCP database, although its current release includes the MRI structural outputs that were obtained using the HCP pipelines for MRI T1 and T2, we have produced a sub-data using the processing pipeline for MRI T1 alone based on Freesurfer and CIFTIFY. This was done to evaluate the differences between the MRI T1 (legacy) and MRI T1/T2 processing paths and to obtain outputs analogous to the legacy HBN and CHBMP databases. It was confirmed through manual inspection that the structural results produced by the T1 alone pipeline (Freesurfer and Ciftify) render similar standards to the structural outputs produced by the HCP T1 and T2 pipeline, given in terms of the brain tissue segmentation.

We processed the HBN dataset with our Ciftify-MEEG pipeline in collaboration with the Child Mind Institute (CMI), where only the T1 MRI was acquired consistently with the EEG recordings. For this reason, the test of the concept followed as a general rule, the HCP-like pipeline branch designed for legacy data (Freesurfer and CIFTIFY). The purpose of the HBN dataset was to investigate brain connectivity and its longitudinal association with clinical and behavioral data. They were attempting to reproduce similar HCP standards. Several neuroimaging modalities (MRI, EEG, fMRI, DWI) and behavioral/clinical data were collected in this database and for a large number of subjects. However, by manual inspection of some of their structural MRI acquisitions and the HCP structural and head modeling outputs produced by our pipelines, we have found that the HBN database quality falls far behind the HCP database standards.

We have found significant artifacts caused by movement and noise in both the T1 and T2 MRIs of the HBN database. For most subjects, the artifacts were quite extended spatially, covering both external and tissue areas. This makes it challenging to judge the cost/benefit relationship in the decision to remove it using any preprocessing. As we explain in the next section, any preprocessing would lead to hollowed MRIs or imperfect segmentation.

The correction for QC indicators in Table 2 the figures 9-16 can be done automatically through quality measures for the detection of distortions in the Lead Field that are produced by geometrical defects in the head model, which have consequences in the accuracy of the OpenMEEG BEM (Gramfort *et al.*, 2010), MEEG Overlapping Spheres (Huang, Mosher and Leahy, 1999) or DUNEuro FEM (Schrader *et al.*, 2021) integrations.

These quality measures (Figure 7) are based on the correlations between the homogeneous Led Field (assuming homogenous conductivity of the head) and the heterogeneous Lead Field (assuming heterogeneous conductivity), estimated with OpenMEEG BEM. Figure 7 shows the bidimensional scatter plot for the pairs (X, Y), corresponding to the homogeneous (X-axis) and heterogenous (Y-axis) Lead Fields a) before and d) after correction. We have found that errors in the computation of the Lead Field are dependent on the relative distance between tissue layers. The relative distance is computed as the minimum distance between the cortex and inner-skull surface meshes. The correlations are then computed for the column vectors of the Lead Field that can be interpreted as the spatial distribution of fields at the sensor space for each generator. See the cortical maps with the correlations of each generator b) before and e) after correction. In this example, the correlation values for the fields computed across sources in a) before correction (spanning between -0.4 to 0.4) change dramatically in c) after correction (above 0.3).

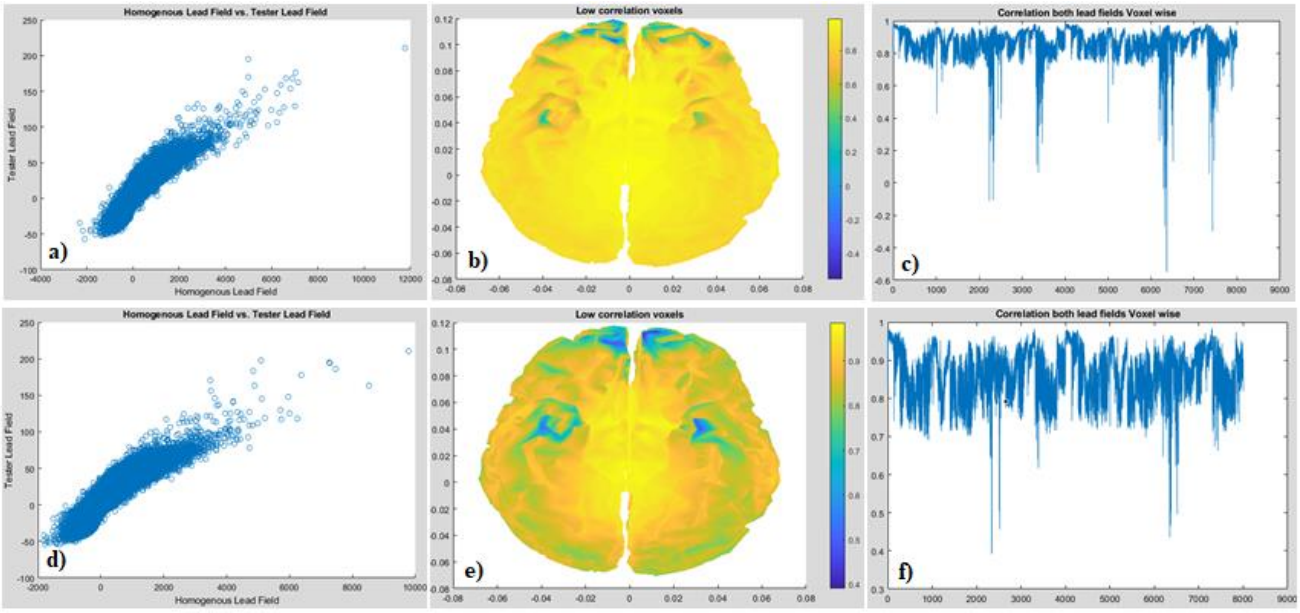

Figure 7 Case example for the quality control of Lead Field, before and after the layer distance correction

The specific artifact in the figure is explained because, for some voxels, the correlation for some voxels in the inferior cortical areas falls below 0.3 (the threshold for weak correlation), as it is shown in the node vise correlation linear plot and cortical topography. After correction (right panel), the minimum correlation appears around the same voxels, but this time above 0.4. The results of the automatic quality control for the Lead Field also interact with the results of the manual quality control for the segmentation of brain and non-brain tissue and sensor registration.

However, this relationship is not trivial because the artifacts in the segmentations and sensor registration are multifactorial and cannot be summarized through a closed group of parameters. Independent work is also being developed to formalize the Lead Field quality control for MEG and EEG based on the relative distance between layers segmentation, included here partially, and the scores for different classifiers of the quality of segmentation and sensor registration reported by experts during the manual quality control.

We have developed a suit for the friendly interaction with the HCP structural pipeline, which is executed by calling the function (HCP_BST_source_head_modeller). See Figure 8 left. This is an open-source suit, written for MATLAB R2020, which can by run in windows and Linux systems and evokes private dependencies of the HCP pipelines of Brainstorm, SPM12, and EEGLAB. If not evoked directly from the pipeline, outputs from the structural HCP pipeline are required formerly for any processing, such as HCP-compatible structural elements (MRI gray matter and head segmentations and atlases) obtained from the MRI preprocessing in two alternative modes.

Mode 1) T1w alone from CIFTIFY preprocessing.

Mode 2) T1w and T2w from preprocessing with the HCP pipeline

Mode 3) Not T1 or T2 from structural Brainstorm template

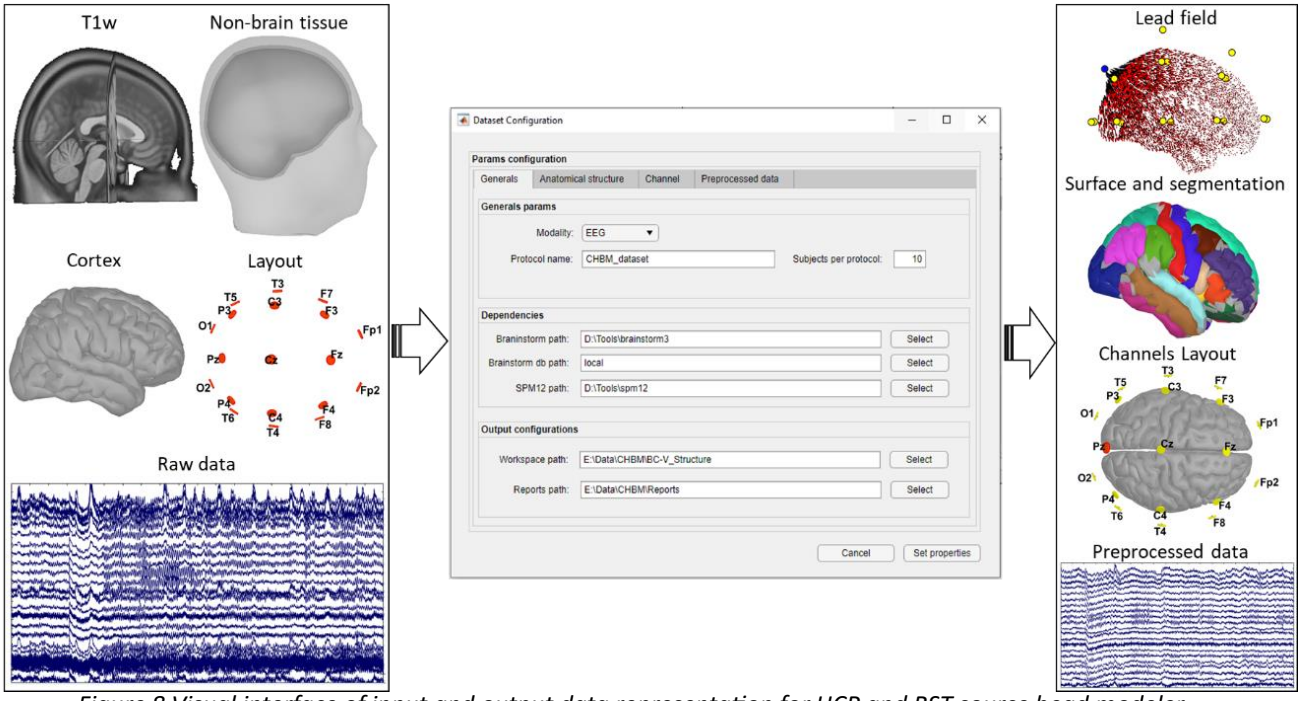

Figure 8 Visual interface of input and output data representation for HCP and BST source head modeler (HCP_BST_source_head_modeler) toolbox.

In addition, information relative to the recordings is necessary (in Brainstorm or EEGLAB compatible format) to incorporate the sensor layout that is used for the construction of the head model and calculation of the Lead Field. Also, the (MEE or EEG) signals if specific preprocessing of the data is desired.

The processing, which can be configured by the user in the interface shown in Figure 8 center, provides visuals about the head model, the cortical segmentation and atlas, the co-registration of the sensors in the scalp surface, the preprocessed data (MEG/EEG) if and the MEG/EEG Lead Fields. These outputs, shown in Figure 8 right, are stored in a standard Brainstorm format that can be read later for the analysis of electrophysiological source imaging and connectivity by the BC-VARETA.

3.2 Concurrent source spectral networks mapping in the HCP (sMRI, MEG), HCP (sMRI, 10-20 system pseudoEEG), and CHBMP (sMRI, 10-05 system EEG) using Ciftify-MEEG and Ciftify-bcVARETA sequential processing

We have designed a simulation package to validate the Electrophysiological Source Imaging and Connectivity methods that use an artificial set of simulations. The "ground truth" for the simulations is, in this case, fixed from an ESI solution obtained from a high-density, high-quality real MEG experiment to establish a landmark—a type of expedient that produces Lead Fields that are better conditioned than those of EEG (Figure 9). This is then used to simulate "pseudo-EEG signals" with a much lower electrode density "and sources reflected on the scalp with a less well-conditioned EEG forward model defined on the same head geometry. Then, the pseudoEEG is inverted to produce the estimated sources that are

compared against the MEG ground truth. The MEG is the ground truth obtained by the primary inverse method Minimum Norm in other to avoid any bias. It does not consider any structural or functional prior.

Our simulation pipeline follows nine steps that are shown in Figure 9:

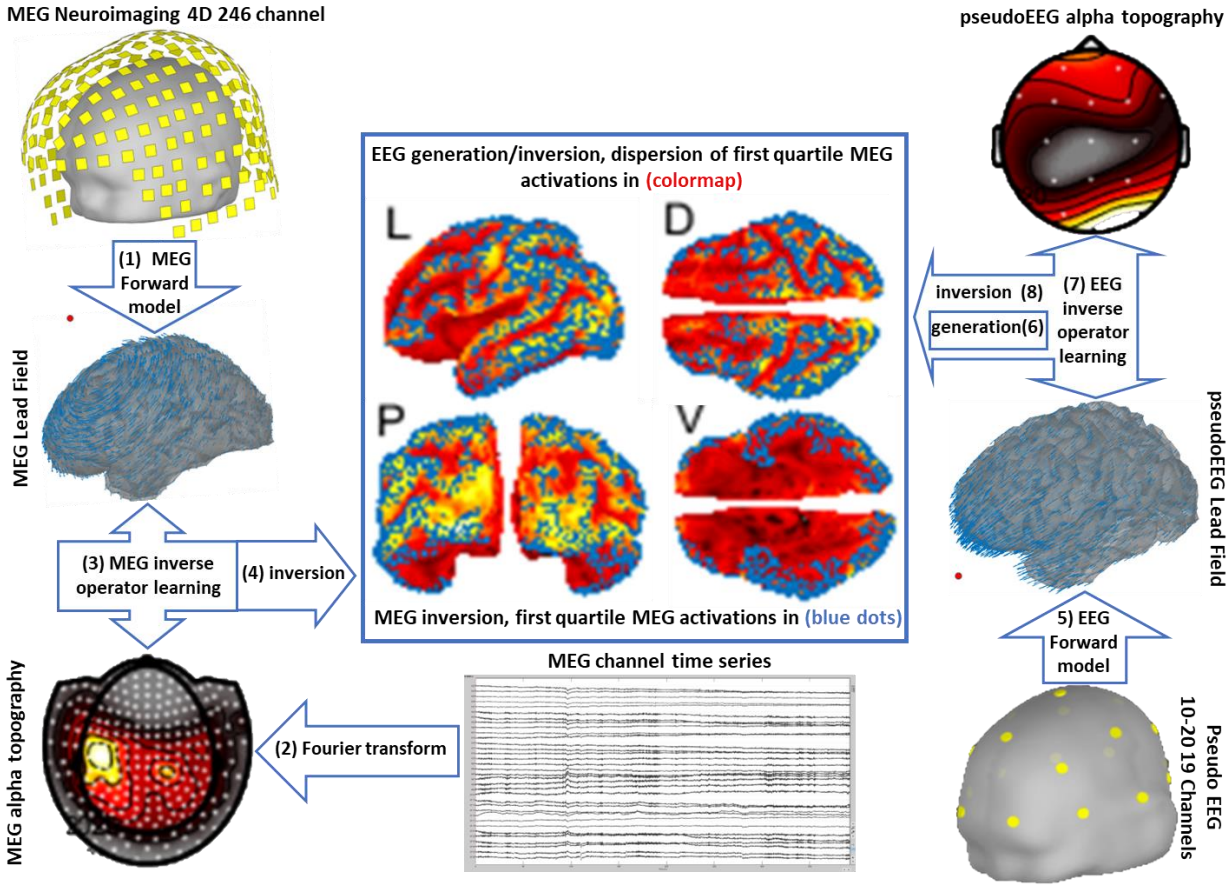

Figure 8 Illustration of pseudoEEG simulation from real MEG sources

Step 1) Extraction of the MEG head model and Lead Field following our Brainstorm pipeline for MEG, which was explicitly designed to utilize the HCP structural data, illustrated in Figure 3 for the HCP subject 175237. The head model included one tissue layer (scalp) extracted with FSL and a grid of 8K generators distributed in the middle layer of the Cortex.

Step 2) The cross-spectra was obtained at a spectral resolution of 0.5Hz from the Fourier Transform (FT) applied to the HCP MEG preprocessed resting data segments recorded at a sampling rate 508Hz. This yielded, in the calculation of the cross-spectra for each HCP subject, a sample number of 1032 or 172(segments)×6(Slepian windows) per frequency bin.

Step 3) MEG inverse modeling of the source transfer operator via the Minimum Norm method, using the average MEG cross-spectra (from step 2) for each frequency band and Lead Field (from step 1). This process used an optimal selection of the Minimum Norm regularization parameters using cross-validation of the solution that best fits the cross-spectra.

Step 4) Inversion to obtain the MEG source cross-spectra for each band from the left and right cross-product of the Minimum Norm transfer operator by the MEG sensor average cross-spectra.

Step 5) Extraction of the EEG head model corresponded to 19 channels from the 10-20 system, also computed following our Brainstorm pipeline for EEG via the Boundary Elements Method. The head model included three tissue layers (inner skull, outer skull, scalp) extracted with FSL, the same grid of 8K generators distributed in the middle layer of the Cortex.

Step 6) Generation of the EEG sensor average cross-spectra for each band from the left and right cross-product of the EEG Lead Field by the source cross-spectra obtained from MEG.

Step 7) EEG inverse modeling of the source transfer operator via the inverse methods (eLORETA, LCMV, sSSBL), using the average EEG cross-spectra (from step 2) for each frequency band and Lead Field (from step 5). This process used an optimal selection of the Minimum Norm regularization parameters by cross-validation of the solution that best fits the cross-spectra.

Step 8) Inversion to obtain the EEG source cross-spectra for each band from the left and right cross-product of the Minimum Norm transfer operator by the pseudoEEG sensor average cross-spectra.

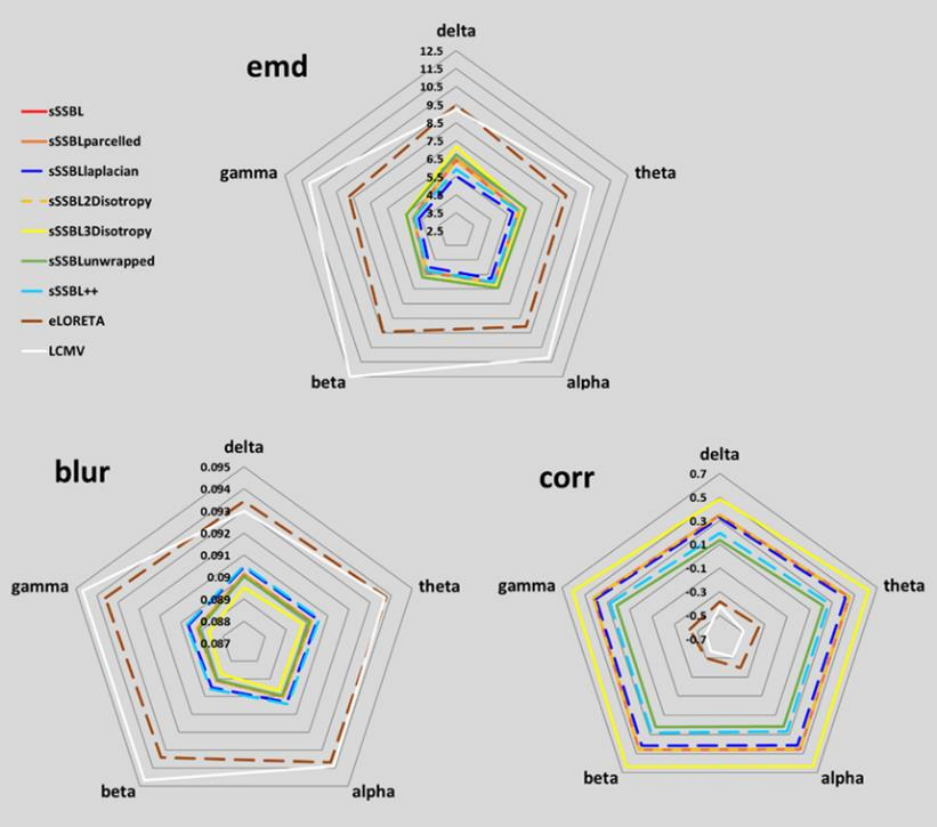

Figure 10 Some quality measures for the source spectra of different bands computed for the outputs of the MEG/pseudoEEG simulation

The process illustrated in Figure 3 was replicated for the whole HCP MEG data (about 70 subjects), producing similar outputs for the real MEG and pseudoEEG: head models, Lead Fields, priors, sensor

cross-spectra, as well as the source transfer operator computed with different methods, which is later used to determine the source cross-spectra spectra, and quality measures of the differences between MEG and EEG sources spectra obtained for five spectral bands.

We have included in our simulation pipeline three different methods for an initial test of the concept of the quality measures for the spectra, eLORETA, LCMV, and sSSBL. This is available on GitHub (https://github.com/CCC-members/HCP-MEGvsEEG_Concurrency). However, the results or open-source code of our pipeline can be easily extended to:

a) Include quality measures to compare MEG/EEG connectivity derived from the cross-spectra obtained with the same methods we have implemented.
b) Include other methods for the comparison of MEG/EEG source spectra or cross-spectra.
c) Perform the statistical comparison of the quality measures for the MEG/EEG spectra or cross-spectra obtained with different methods.

See an instance of the quality measures reported for the MEG of subject 175237 in Figure 10. We remind the reader that we measure leakage through the Spatial Dispersion (SD) of the PSF for the EEG solution (BLUR) and concurrency through the surface-based Earth Mover's Distance (EMD) correlation (CORR) between the MEG-based and EEG-based spectra. Also, several different variants of sSSBL were explored to see the effect of different proposed structural priors. We remind the reader that these priors incorporate additional information (structural or functional) on the spectral activity. Namely sSSBL (no prior), sSSBLparcelled (cortical parcellation information), sSSBLlaplacian (Laplacian smooth operator), sSSBL2Disotropy (2D rotational invariance), sSSBL3Disotroopy (3D rotational invariance) and sSSBLunwrapped (surface curvature compensation). SSBL++.

We have consistently compared the MEG/EEG populational spectral using our pipelines. The MEG and EEG were acquired in different populations conforming to the public databases: MEG of the Human Connectome Project (HCP) and EEG of the Cuban Human Brain Mapping (CHBM). For both databases, we have obtained the outputs of our pipelines, which would allow comparing not only functional features (such as spectra and cross-spectra) between the populations but also structural ones. We illustrate some of the results with this application of our pipelines for a sample of 45 cases of MEG and EEG considered to test the following hypothesis "the spatial distribution of power amplitude for the generators of MEG and EEG are expected to be same."

For each dataset (MEG or EEG), this type of analysis yielded a 3D array J of dimension $(Ng\ x\ Nf\ x\ Ns)$, where Ng indicates the number of possible generators, Nf is the number of oscillatory frequencies considered in the analysis, and Ns is the number of subjects. Note that the comparison of sources was limited to cortical areas following our HCP-compliant pipeline. The frequencies under study were limited to the bands: Delta, Alpha, Theta, Beta, and Gamma-low, to exclude part of the spectra (Gamma-high) that was altered by the preprocessing. Before any statistical comparison, we removed the effect of two factors, which may introduce populational differences in the power amplitude of MEG/EEG generators:

Factor 1) the frequency-dependent scale difference between the global amplitudes of the generators estimated from MEG and EEG. To rule out this effect, we modeled a populational scale factor representing the spectral differences reported for the simultaneous MEG/EEG recordings (Dehghani *et al.*, 2010) introduced during the preprocessing.

Factor 2) the different decay regimes for the amplitude of MEG and EEG generators with the cortical deepness, which is also the cause for the additional visibility of MEG/EEG sources (Piastra *et al.*, 2021). To rule out this effect, we model a populational exponent representing the contraction of visibility with cortical deepness.

Effects a) and b) can be represented combinedly as (given in MATLAB notation):

$$\mathrm{JMEG}(:,\mathrm{f}) = \mathrm{e}^{\mathrm{a(f)}} \cdot \mathrm{JEEG}\,(:,\mathrm{f})^{\mathrm{b(f)}}$$

- $\mathrm{JMEG}(:,\mathrm{f})$ and $\mathrm{JEEG}(:,\mathrm{f})$ denote the vectors of populational amplitudes for the MEG and EEG generators at the frequency indexed f.

- $a(f)$ is the frequency-dependent logarithmic scale difference (for convenience, we use $\mathrm{e}^{\mathrm{a(f)}}$ as the current scale factor).

- $b(f)$ is the frequency-dependent exponential contraction in the spatial distribution.

To illustrate the concurrency and possible differences between the MEG and EEG source spectra, we represent in 3D scatter plots the populational values of the source log-spectra for MEG and EEG against frequency (from 0Hz to 40Hz), see Figure 11abc.

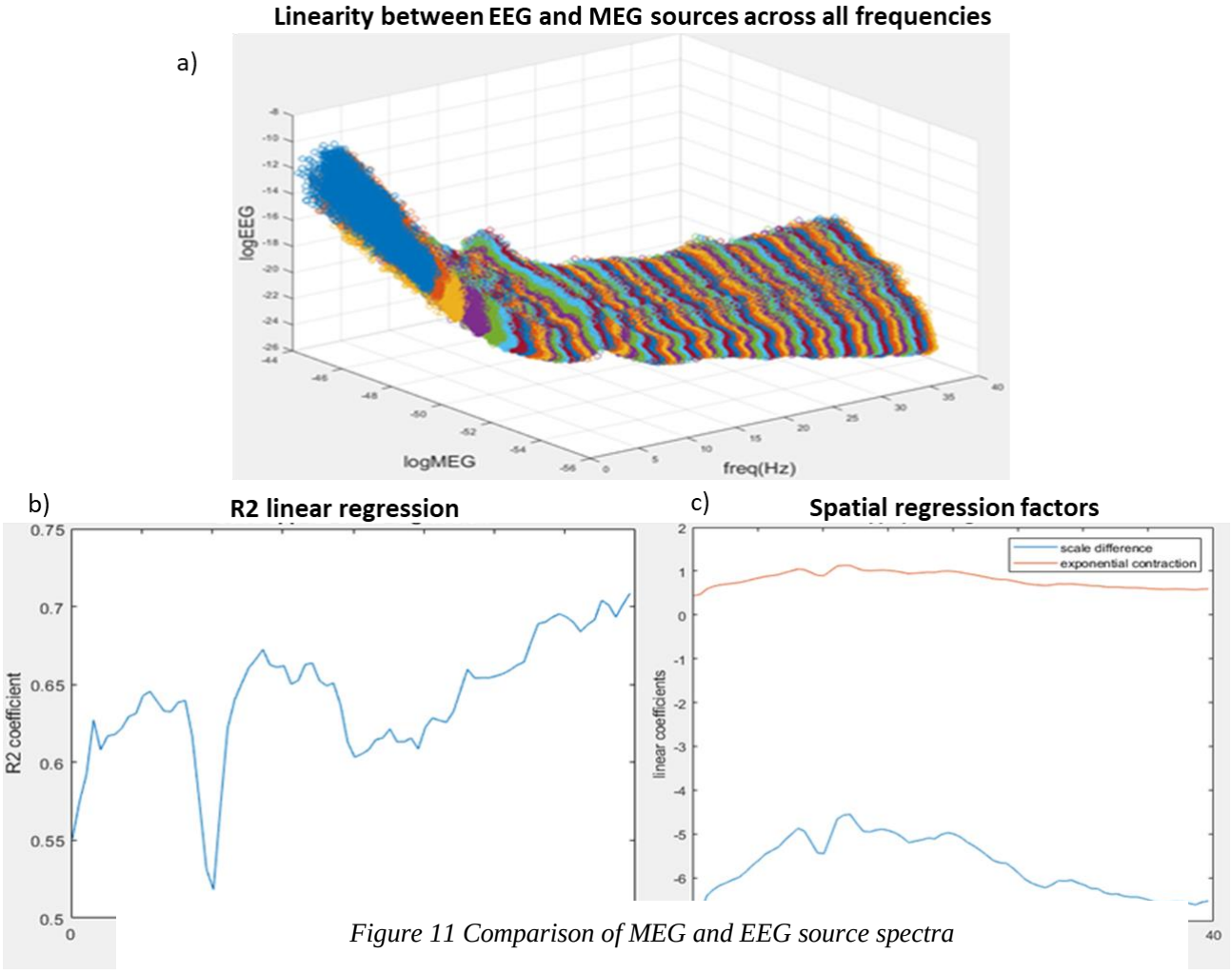

Figure 11 Comparison of MEG and EEG source spectra

Where the source log spectra were computed with sSSBL (Figure 11a). Figure 10a suggests that $logMEG$ and $logEEG$ keep up a place in some linear proportion, which we analyze quantitatively through the R2 coefficients in Figure 10b. However, the proportion suffers from significant variations along frequency. Figure 11c shows the plots with the frequency-dependent baseline (logarithmic scale difference) and slope (exponential contraction) difference for the log-spectra.

In Figure 12, we illustrate the results of the statistical comparison between MEG and EEG source spectra in 3D cortical topographies (at 8K resolution) for five bands (delta, theta, alpha, beta, and gamma-low). Note that the differences under evaluation exclude a populational scale factor, and exponential contraction, which we have acknowledged beforehand, is an irremediable source of differences. The topographic plot shows the indicator function $1(\Omega\ (f1, f2))$, where $\Omega\ (f1, f2)$ is the set containing those generators in the range of frequencies $f1 - f2$ yielded significant differences. The reported differences correspond to the values over threshold $th(\alpha)$ of the t-statistic $T * (g, f)$, where the threshold is the interpolated value in the empirical distribution of the t-statistic $T(g, f)$, determined in permutations of the MEG/EEG cases, at a level of significance α.

$$\Omega\ (f1, f2)\ =\ Uf = f1{:}\ f2\{g|abs(T * (g, f))\ >\ th(\alpha)\}$$

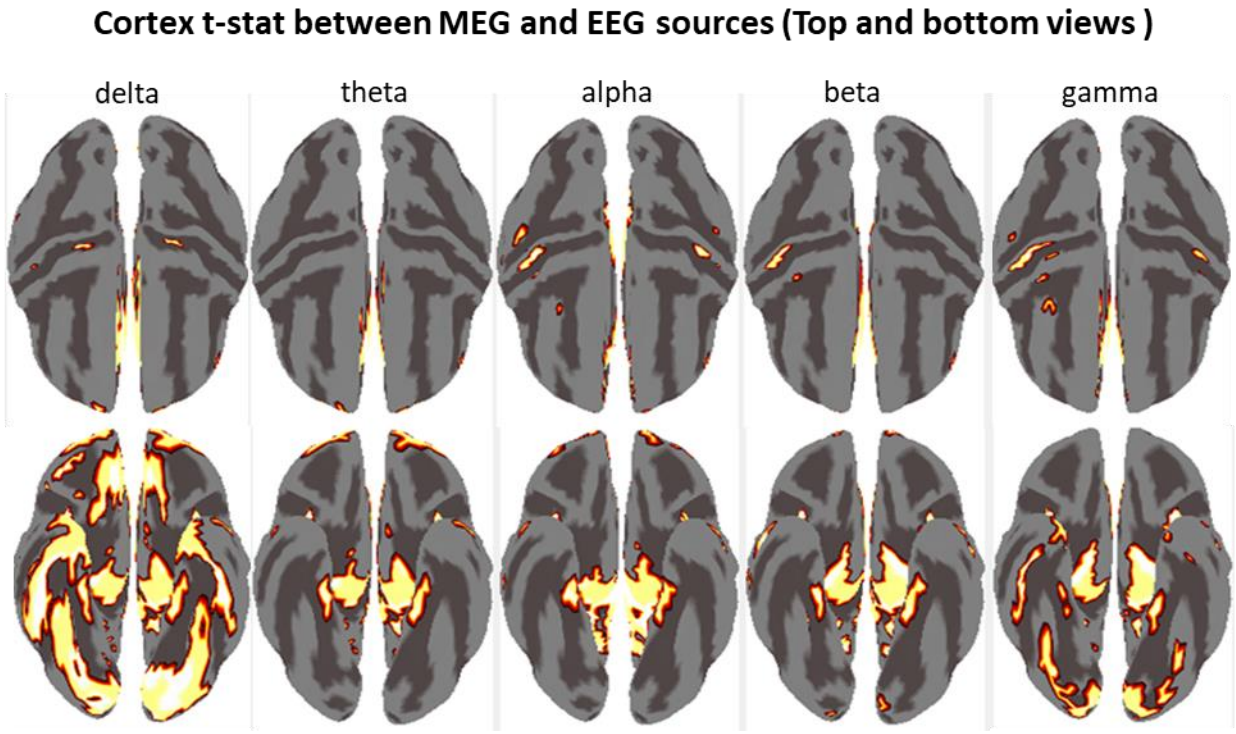

Figure 12 Statistical test for differences between the MEG/EEG source spectra in the HCP and CHBM database

The areas marked in white represent the value 1 for the indicator function of the set $\Omega\ (f1, f2)$ $(1(\Omega\ (f1, f2))\ =\ 1)$, which means at least for a particular frequency between $f1$ and $f2$ a significant difference was expressed for the MEG and EEG in the power amplitude of the given gene

We have developed a suit based on MATLAB 2020 to analyze MEG/EEG data with BC-VARETA. Different tabs in the suit allow the selection of the level of analysis desired by the user, in hierarchical order 1) "sensor level", MEG/EEG signal spectra, cross-spectral tensor, and spectral precision tensor 2) "activation

level", MEG/EEG source space spectra, 3) "connectivity level", MEG/EEG source space cross-spectral tensor and spectral precision tensor. Note that the hierarchy in the "analysis levels" must be respected, and therefore executing any level required to be maintained with the outputs of the previous one.

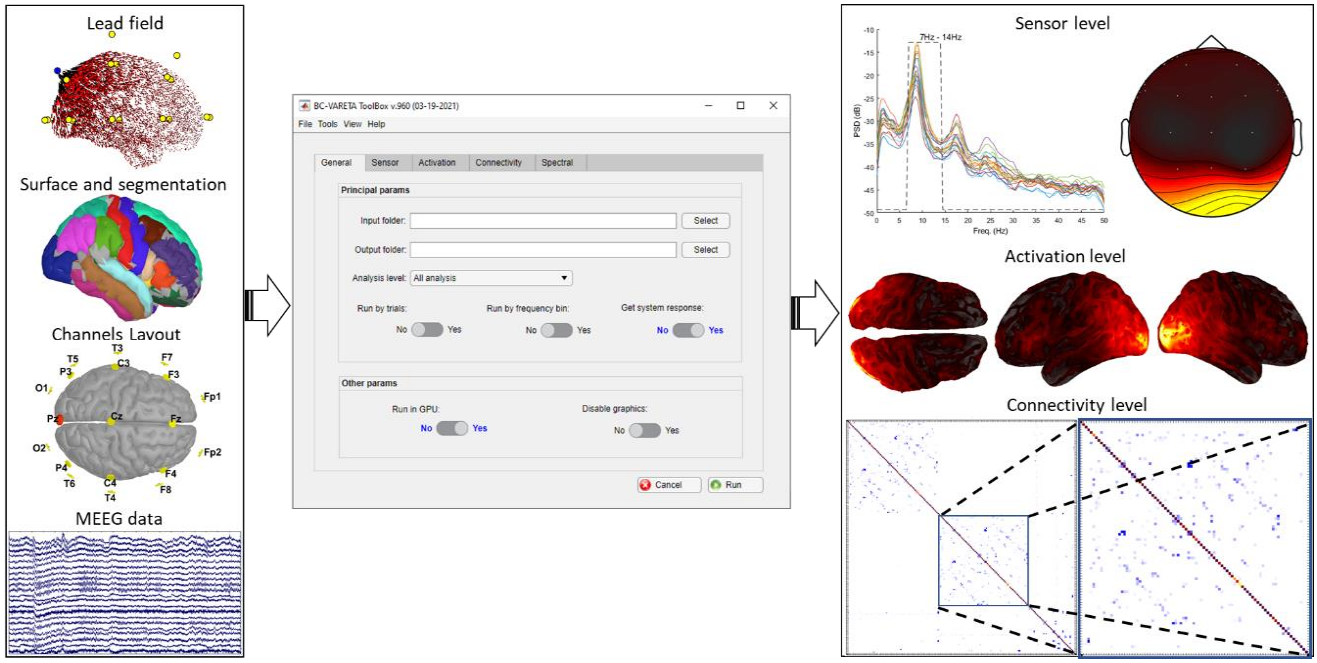

Figure 13 General tab in the visual interface of the BC-VARETA Toolbox

4 Discussion

The strategy of surface-based signal extraction produces more interpretable results, acknowledging the layer (surface) specific nature of neural processes that occur in the Cortex at the mesoscopic (millimetric) scale, which are involved in the generation of cortical fMRI (Poplawsky, Fukuda and Kim, 2019) and external MEG/EEG recordings (Nunez *et al.*, 1994). These processes have a common origin in the postsynaptic potentials (PSP) (Freeman, 1975; Nunez *et al.*, 1994; Valdes-Sosa *et al.*, 2009).

It has been demonstrated the increased specificity of surface-based processing in separating the proper cortical fMRI signals from the noise, which can reach up to 1dB, or noncortical fMRI signals (Dale *et al.*, 2000; Das *et al.*, 2012; Amunts *et al.*, 2013; Lopes da Silva, 2013; Marcus *et al.*, 2013; Van Essen *et al.*, 2013; Sherif *et al.*, 2014; Helbling *et al.*, 2015; Esteban *et al.*, 2019; Halgren *et al.*, 2019; Xiao *et al.*, 2019).

Source modeling based on cortical generators dramatically improves the conditioning of the Lead Field matrix (Nunez *et al.*, 1994; Larson-Prior *et al.*, 2013), affecting inverse methods and allowing practicing electrophysiological source imaging at a resolution that is comparable with other techniques such as fMRI (Brookes *et al.*, 2011; Hall *et al.*, 2014).

Cortically mapped structural connectivity that is extracted from the dMRI tractography, in combination with information fMRI or MEG connectivity or functional cortical parcellations extracted from fMRI,

provides an unprecedented level of detail in mapping cortical connectomes that are relevant for the study of brain function (Wang, Yoldemir and Abugharbieh, 2015; Vassal *et al.*, 2016).

Our contribution is an HCP-compatible MEG and EEG source processing pipeline (HCP-MEEG). This is based on HCP-like structural MRI (sMRI) processing (Van Essen *et al.*, 2013) and Brainstorm MEG/EEG source/head modeling (Tadel *et al.*, 2011), we achieve quality ensured computation of the Lead Field; for both EEG and MEG. The sMRI processing for the obtention is based on the HCP structural pipeline for cases that include T1 and T2 MRIs, CIFTIFY pipeline (Dickie *et al.*, 2019) for subjects with only T1 MRIs and Brainstorm structural template for those does not have T1 and T2 MRIs. Code with batch processors that produces the geometrical structures and Lead Field, which invokes the HCP structural pipeline, CIFTIFY, and source/head modeler based on FSL and the Brainstorm suit, is freely available in GitHub.

1) Dependency of this pipeline to HCP source and head model outputs that are computed by Fieldtrip and the specific 4D neuroimaging MEG data registered with the head model.

2) High-level programming that introduces dependency from specific Brainstorm configuration for the geometric processing and Lead Field computations.

Therefore, we have developed an open pipeline at the level of Brainstorm head modeler and added several functionalities that bring several significant advantages.

3) Batch processing of Lead Field with user-defined options that can be changed for the specific databases using JSON configuration files.

4) Directly reading the HCP (Glasser *et al.*, 2013; Van Essen *et al.*, 2013), Ciftify (Dickie *et al.*, 2019) or Freesurfer (Fischl, 2012), and FSL (Smith *et al.*, 2004; Woolrich *et al.*, 2009; Jenkinson *et al.*, 2012) structural outputs and customized construction of the MEG/EEG source and head models.

5) Plugging additional functionalities, such as a quality control loop and FSAverage registration, that were written to optimize this pipeline and from different standard processing tools based on MATLAB, such as Fieldtrip and SPM.

6) Configurable geometric processes optimized according to each database's defects, which follow different processing paths in our pipeline.

7) Direct interaction through an open parametrization of the functions for Lead Field computations that can be obtained with SPM, BST code, Fieldtrip, and OpenMEEG BEM (Gramfort *et al.*, 2010) or DUNEuro FEM (Schrader *et al.*, 2021).

Were processed 1251 sMRI from the CMI dataset with our structural processing pipeline getting the layer segmentation, the sensor layout registration, the head model, and the Lead Field. These results were subjected to visual quality control, obtaining 60 Lead Fields marked as doubtful and the rest as good. All 60 LFs declared as "doubtful," and another 40 goods LF samples from the 1251 LFs of the CMI dataset were used as the sample in the Automatic Quality Control of the numerical accuracy of EEG Lead Fields (LF-AQI) (Vega *et al.*, 2021). This analysis found three main reasons why the LFs were screened as "doubtful": the first reason was the blurred/noisy in the MRI causing inaccurate segmentation, the second one was an evident misalignment of the Cortex inside the head, and the bad alignment of the sensor's layout caused thirst.

In case of incorrectly segmented MRIs, we first try to reperform the MRI segmentation steps to achieve proper segmentation. However, in cases where MRIs still cannot be adequately segmented, we proceed by rejecting the subject and marked as bad from HCP structural outputs and FSL nonbrain tissue of individual processing with chosen structural template outputs. The templates are useable to perform approximated electrophysiological source imaging from the EEG. A specific parameter in the pipeline configuration files allows switching individualized or predetermined template anatomy to facilitate this process. This feature helps correct the second type of artifact we found in the "to-be-checked" labeled LFs. The last correction is to update the sensor layout. Since we have already performed automatic sensor correction during the head modeling step, we manually correct the electrode alignment and placement on the scalp and recompute the Lead Field again after the manual correction and processed by the after-manual-quality-control process. Once the corrections were completed, the LFs marked as bad were passed through the LF-AQI pipeline (Vega *et al.*, 2021), getting all then corrected and declared as goods, and LF-AQI then accepted these LFs.

The processing done with our HCP-compatible pipeline and the source spectra with the BC-VARETA Toolbox of EEG data from the CHBM dataset (Valdes-Sosa et al., 2021) and the MEG data from the HCP dataset (Van Essen *et al.*, 2013) were used to validate the Stepwise Covariance-Free Common Principal Components (CF-CPC) (Riaz et al., 2021) extracting the shared anatomical structure of EEG and MEG source spectra across a frequency range of 0.01–40 Hz from 45 subjects of each group

The forward model and source spectra obtained by our structural HCP-compatible pipeline and BC-VARETA Toolbox, respectively, from the EEG of 70 subjects from the Cuban Human Brain Mapping project and the MEG of 70 subjects from the Human Connectome Project were used to perform a statistical comparison between the sources of EEG and MEG rhythms (Riaz *et al.*, 2020)

Our BC-VARETA Toolbox was used to analyze the EEG source activity and functional connectivity to explore the feasibility of functional connectivity under aggravating conditions for the spatial resolution of EEG source analysis commonly found in clinical settings. This study (González-López *et al.*, 2022) uses EEGs with a limited number of channels (19 channels) to obtain the inverse problem solution. This proves that BC-VARETA Toolbox is feasible and can be used in clinical settings since it involves significantly lower costs than other neuroimaging tools and can be employed using standard 19-leads EEG to assess brain connectivity.

5 Conclusions

1) We have developed a pipeline that follows the Human Connectome Project (HCP) standards for extracting source models, head models, and Lead Fields in legacy databases. This is a continuation of the work developed by the HCP team, which was based before on a specific type of Fieldtrip processing for the obtention of MEG source and head models, from specific geometric files that are obtained as a post-processing of the HCP (structural) outputs. The MEG source and head modeling pipeline introduced by the HCP would be impractical for legacy databases containing EEG data or different geometric files. As we have shown, source models, head models, and Lead Fields are extracted with our pipeline for multiple types of MEG/EEG databases, which might contain or not the structural images that are used to define the geometry. For this, we have used the Brainstorm suit, which previously included a pipeline for Lead Field computation based on the same HCP geometric model produced by Fieldtrip.

2) In our pipeline, we have substituted the Fieldtrip processing with some modules that produce analogous geometric files that are needed for Lead Field computations. The obtention of HCP-like structural outputs in legacy databases, which may contain structural Magnetic Resonance Imaging (sMRI) T1, or alternatively T1&T2 according to HCP acquisition protocols, was possible by means of our preprocessing pipeline geared to the Brainstorm source modeling pipeline. By means of CIFTIFY, a suit designed for sMRI T1 legacy imaging data, and the HCP structural pipeline, whereas T1 and T2 are available, we have produced HCP structural outputs that are plugged in both cases into the MEG/EEG source and head modeling pipeline.

3) Our pipeline for source and head modeling also produced the quality control indicators to assess the quality of the Lead Field based on the geometric outputs for 1) head modeling, upon a head tissue segmentation extracted with FSL, 2) source modeling, upon HCP anatomy extracted with CIFTIFY or HCP pipelines. By visual inspection of an Html file, the cases can be classified to be corrected following three different paths 1) Substitution of files with geometric defects that can be processed by other means. 2) Manual correction of the geometric defects in the sensor layout. 3) Automatic correction of geometric defects in the tissue layers.

4) We have introduced present a pipeline: Brain Connectivity Variable Resolution Tomographic Analysis (BC-VARETA): a tool for electrophysiological source imaging and connectivity that is designed with Bayesian methods to map brain networks that emerge from specific oscillatory activity (network spectral topographies and topologies). Mapping brain network topographies and topologies via the MEEG sensor time-series statistics has been a persistent fallacy. Existent alternatives to mapping such networks are Step 1) Inversion of the MEG/EEG Lead Field to obtain source time series and the topography of networks; Step 2) Determination of their connectivities or topology. This would seem flawed due to the effect of distortions (localization error and blurring) that originate from the Lead Field's ill-conditioning, affecting both the estimated topographies and topologies. Our pipeline incorporates libraries with methods designed to solve these problems, Library 1) Spectral Structured Sparse Bayesian Learning method (sSSBL) for the estimation of sparse network topographies. Library 2) Hidden Gaussian Graphical State-Space model (HIGGS) with Hermitian graphical LASSO prior, for the estimation of sparse topologies. In addition, to compensate for the bias of sparsity in the estimated networks, we leveraged fused sparsity with weight coefficients designed to incorporate cortical priors. These priors included compensation of depth based upon cortical curvature, the neighbor structure cortical Laplacian, and the rotational invariance of cortical Lead Fields.

5) We have introduced a configurable pipeline used to validate the BC-VARETA toolbox and investigate the limitations of other state-of-the-art methods under different conditions. This pipeline evaluates the consistency of electrophysiological source imaging and connectivity methods, and their priors, in inverting different source models, head models, and Lead Fields, which are used to simulate sensor signals based on synthetic brain spectral topographies and topologies. This concept was extended with a pipeline that uses a ground truth based on high-density HCP MEG data to generate low-density pseudoEEG to challenge the capability under extreme conditions. This is a rather extensible validation procedure designed to produce inverse solutions with pseudoEEG and their statistics for the HCP MEG database. This type of validation shall be used in the future to analyze the distortions of network spectral topographies and topologies produced by different methods and explore the possible solutions to this problem with priors, more realistically.

Conclusion 6) BC-VARETA has produced source spectral topographies and topologies with unprecedented quality in this type of simulation. However, this pipeline would test several configurations that are not included in this work and might be relevant for real studies. We also prepared a release with HCP-compatible and concurrent electrophysiological source imaging and connectivity data obtained with BC-VARETA, for the Human Connectome Project MEG and the Cuban Human Brain Mapping Project EEG. The results of BC-VARETA confirm our expectations based on the previous validation using real MEG and pseudoEEG. The source topographies for MEG and EEG were compared via permutation tests, yielding striking similarities between either technique and only a few differences associated with the low sensitivity of EEG to detect subcortical and interhemispheric sources.

6 Reference

Akalin Acar, Z. and Makeig, S. (2013) 'Effects of forward model errors on EEG source localization', *Brain Topography*, 26(3), pp. 378–396. Available at: https://doi.org/10.1007/s10548-012-0274-6.

Alexander, L.M. *et al.* (2017) 'An open resource for transdiagnostic research in pediatric mental health and learning disorders', *Scientific Data*, 4(1), p. 170181. Available at: https://doi.org/10.1038/sdata.2017.181.

Amunts, K. *et al.* (2013) 'BigBrain: An Ultrahigh-Resolution 3D Human Brain Model', *Science*, 340(6139), pp. 1472–1475. Available at: https://doi.org/10.1126/science.1235381.

Anticevic, A. *et al.* (2008) 'Comparing surface-based and volume-based analyses of functional neuroimaging data in patients with schizophrenia', *NeuroImage*, 41(3), pp. 835–848. Available at: https://doi.org/10.1016/j.neuroimage.2008.02.052.

Avants, B.B., Tustison, N. and others (2014) 'Advanced normalization tools (ANTS)'.

Bonaiuto, J.J. *et al.* (2018) 'Non-invasive laminar inference with MEG: Comparison of methods and source inversion algorithms', *NeuroImage*, 167(November 2017), pp. 372–383. Available at: https://doi.org/10.1016/j.neuroimage.2017.11.068.

Brodoehl, S. *et al.* (2020) 'Surface-based analysis increases the specificity of cortical activation patterns and connectivity results', *Scientific Reports*, 10(1), p. 5737. Available at: https://doi.org/10.1038/s41598-020-62832-z.

Brookes, M.J. *et al.* (2011) 'Investigating the electrophysiological basis of resting state networks using magnetoencephalography', *Proceedings of the National Academy of Sciences*, 108(40), pp. 16783–16788. Available at: https://doi.org/10.1073/pnas.1112685108.

Buxhoeveden, D.P. and Casanova, M.F. (2002) 'The minicolumn hypothesis in neuroscience', *Brain*, 125(5), pp. 935–951. Available at: https://doi.org/10.1093/brain/awf110.

Cheng, A.H.-D. and Cheng, D.T. (2005) 'Heritage and early history of the boundary element method', *Engineering analysis with boundary elements*, 29(3), pp. 268–302.

Coalson, T.S., Van Essen, D.C. and Glasser, M.F. (2018) 'The impact of traditional neuroimaging methods on the spatial localization of cortical areas', *Proceedings of the National Academy of Sciences*, 115(27). Available at: https://doi.org/10.1073/pnas.1801582115.

Dale, A.M. *et al.* (2000) 'Dynamic Statistical Parametric Mapping', *Neuron*, 26(1), pp. 55–67. Available at: https://doi.org/10.1016/S0896-6273(00)81138-1.

Dale, A.M., Fischl, B. and Sereno, M.I. (1999) 'Cortical Surface-Based Analysis', *NeuroImage*, 9(2), pp. 179–194. Available at: https://doi.org/10.1006/nimg.1998.0395.

Dannhauer, M. *et al.* (2011) 'Modeling of the human skull in EEG source analysis', *Human Brain Mapping*, 32(9), pp. 1383–1399. Available at: https://doi.org/10.1002/hbm.21114.

Dannhauer, M. *et al.* (2012) 'A pipeline for the simulation of transcranial direct current stimulation for realistic human head models using SCIRun/BioMesh3D', *Proceedings of the Annual International Conference of the IEEE Engineering in Medicine and Biology Society, EMBS*, pp. 5486–5489. Available at: https://doi.org/10.1109/EMBC.2012.6347236.

Das, S. *et al.* (2012) 'LORIS: a web-based data management system for multi-center studies', *Frontiers in Neuroinformatics*, 5. Available at: https://doi.org/10.3389/fninf.2011.00037.

Dehghani, N. *et al.* (2010) 'Comparative power spectral analysis of simultaneous elecroencephalographic and magnetoencephalographic recordings in humans suggests non-resistive extracellular media', *Journal of Computational Neuroscience*, 29(3), pp. 405–421. Available at: https://doi.org/10.1007/s10827-010-0263-2.

Dickie, E.W. *et al.* (2019) 'Ciftify: A framework for surface-based analysis of legacy MR acquisitions', *NeuroImage*, 197, pp. 818–826. Available at: https://doi.org/10.1016/j.neuroimage.2019.04.078.

Esteban, O. *et al.* (2019) 'fMRIPrep: a robust preprocessing pipeline for functional MRI', *Nature Methods*, 16(1), pp. 111–116. Available at: https://doi.org/10.1038/s41592-018-0235-4.

Fischl, B. (2012) 'FreeSurfer', *NeuroImage*, 62(2), pp. 774–781. Available at: https://doi.org/10.1016/j.neuroimage.2012.01.021.

Freeman, W.J. (1975) *Mass action in the nervous system : examination of the neurophysiological basis of adaptive behavior through the EEG*. New York ; London: Academic Press.

Friston, K. *et al.* (2008) 'Multiple sparse priors for the M/EEG inverse problem', *NeuroImage*, 39(3), pp. 1104–1120. Available at: https://doi.org/10.1016/j.neuroimage.2007.09.048.

Glasser, M.F. *et al.* (2013) 'The minimal preprocessing pipelines for the Human Connectome Project', *NeuroImage*, 80, pp. 105–124. Available at: https://doi.org/10.1016/j.neuroimage.2013.04.127.

Glasser, M.F. *et al.* (2016) 'A multi-modal parcellation of human cerebral cortex', *Nature*, 536(7615), pp. 171–178. Available at: https://doi.org/10.1038/nature18933.

González-López, M. *et al.* (2022) 'Who's driving? The default mode network in healthy elderly individuals at risk of cognitive decline', *Frontiers in Neurology* [Preprint]. Available at: https://doi.org/doi.org/10.3389/fneur.2022.1009574.

Gonzalez-Moreira, E. *et al.* (2020) *Bottom-up control of leakage in spectral electrophysiological source imaging via structured sparse bayesian learning*, p. 52. Available at: https://doi.org/10.1101/2020.02.25.964684.

Gramfort, A. *et al.* (2010) 'OpenMEEG: opensource software for quasistatic bioelectromagnetics', *BioMedical Engineering OnLine*, 9(1), p. 45. Available at: https://doi.org/10.1186/1475-925X-9-45.

Grech, R. *et al.* (2008) 'Review on solving the inverse problem in EEG source analysis', *Journal of NeuroEngineering and Rehabilitation*, 5(1), p. 25. Available at: https://doi.org/10.1186/1743-0003-5-25.

Halgren, M. *et al.* (2019) 'The generation and propagation of the human alpha rhythm', *Proceedings of the National Academy of Sciences*, 116(47), pp. 23772–23782. Available at: https://doi.org/10.1073/pnas.1913092116.

Hall, E.L. *et al.* (2014) 'The relationship between MEG and fMRI', *NeuroImage*, 102(P1), pp. 80–91. Available at: https://doi.org/10.1016/J.NEUROIMAGE.2013.11.005.

Hallez, H. *et al.* (2007) 'Review on solving the forward problem in EEG source analysis.', *Journal of neuroengineering and rehabilitation*, 4, p. 46. Available at: https://doi.org/10.1186/1743-0003-4-46.

Hämäläinen, M. *et al.* (1993) 'Magnetoencephalography—theory, instrumentation, and applications to noninvasive studies of the working human brain', *Reviews of modern Physics*, 65(2), p. 413.

Hämäläinen, M.S. and Ilmoniemi, R.J. (1994) 'Interpreting magnetic fields of the brain: minimum norm estimates', *Medical & Biological Engineering & Computing*, 32(1), pp. 35–42. Available at: https://doi.org/10.1007/BF02512476.

Harwell, J., Bremen, H., Coulon, O., Dierker, D., Reynolds, R.C., Silva, C., Teich, K., Van Essen, D.C., Warfield, S.K. and Saad, Z.S. (2008) 'GIfTI: geometry data format for exchange of surface-based brain mapping data.', *OHBM–Poster Presentation* [Preprint].

He, B. *et al.* (2019) 'Electrophysiological Brain Connectivity: Theory and Implementation', *IEEE Transactions on Biomedical Engineering*, 66(7), pp. 2115–2137. Available at: https://doi.org/10.1109/TBME.2019.2913928.

He, B., Ding, L. and Sohrabpour, A. (2020) 'Electrophysiological Mapping and Source Imaging', in B. He (ed.) *Neural Engineering*. Cham: Springer International Publishing, pp. 379–413. Available at: https://doi.org/10.1007/978-3-030-43395-6_13.

Helbling, S. *et al.* (2015) 'Structure predicts function: Combining non-invasive electrophysiology with in-vivo histology', *NeuroImage*, 108, pp. 377–385. Available at: https://doi.org/10.1016/j.neuroimage.2014.12.030.

Henson, R.N. *et al.* (2019) 'Multimodal Integration of M/EEG and f/MRI Data in SPM12', *Frontiers in Neuroscience*, 13. Available at: https://doi.org/10.3389/fnins.2019.00300.

Huang, M.X., Mosher, J.C. and Leahy, R.M. (1999) 'A sensor-weighted overlapping-sphere head model and exhaustive head model comparison for MEG', *Physics in Medicine and Biology*, 44(2), pp. 423–440. Available at: https://doi.org/10.1088/0031-9155/44/2/010.

Jackson, E.F. *et al.* (1997) 'A review of MRI pulse sequences and techniques in neuroimaging', *Surgical Neurology*, 47(2), pp. 185–199. Available at: https://doi.org/10.1016/S0090-3019(96)00375-8.

Jenkinson, M. (2005) 'NIfTI-1 Data Format — Neuroimaging Informatics Technology Initiative', *Neuroimaging* [Preprint]. Available at: https://nifti.nimh.nih.gov/nifti-1.

Jenkinson, M. *et al.* (2012) 'FSL', *NeuroImage*, 62(2), pp. 782–790. Available at: https://doi.org/10.1016/j.neuroimage.2011.09.015.

Larson-Prior, L.J. *et al.* (2013) 'Adding dynamics to the Human Connectome Project with MEG', *NeuroImage*, 80, pp. 190–201. Available at: https://doi.org/10.1016/j.neuroimage.2013.05.056.

Lin, F.-H. *et al.* (2008) 'Linear constraint minimum variance beamformer functional magnetic resonance inverse imaging', *NeuroImage*, 43(2), pp. 297–311. Available at: https://doi.org/10.1016/j.neuroimage.2008.06.038.

Lopes da Silva, F. (2013) 'EEG and MEG: Relevance to Neuroscience', *Neuron*, 80(5), pp. 1112–1128. Available at: https://doi.org/10.1016/j.neuron.2013.10.017.

MacKay, D.J.C. (2003) *Information theory, inference and learning algorithms*. Cambridge: Cambridge University Press.

Marcus, D.S. *et al.* (2013) 'Human Connectome Project informatics: Quality control, database services, and data visualization', *NeuroImage*, 80, pp. 202–219. Available at: https://doi.org/10.1016/j.neuroimage.2013.05.077.

Mattout, J. *et al.* (2006) 'MEG source localization under multiple constraints: an extended Bayesian framework', *NeuroImage*, 30(3), pp. 753–767.

McLachlan, G.J. and Krishnan, T. (2007) *The EM algorithm and extensions*. John Wiley & Sons.

Nagasaka, Y., Shimoda, K. and Fujii, N. (2011) 'Multidimensional recording (MDR) and data sharing: an ecological open research and educational platform for neuroscience', *PloS one*, 6(7), p. e22561.

Neal, R.M. (1998) ‘Assessing relevance determination methods using DELVE’, *Nato Asi Series F Computer And Systems Sciences*, 168, pp. 97–132.

Nolte, G. *et al.* (2020) ‘Mathematical Relations Between Measures of Brain Connectivity Estimated From Electrophysiological Recordings for Gaussian Distributed Data’, *Frontiers in Neuroscience*, 14. Available at: https://doi.org/10.3389/fnins.2020.577574.

Nolte, G. and Dassios, G. (2005) ‘Analytic expansion of the EEG lead field for realistic volume conductors’, *Physics in Medicine and Biology*, 50(16), pp. 3807–3823. Available at: https://doi.org/10.1088/0031-9155/50/16/010.

Nunez, P.L. *et al.* (1994) ‘A theoretical and experimental study of high resolution EEG based on surface Laplacians and cortical imaging’, *Electroencephalography and Clinical Neurophysiology*, 90(1), pp. 40–57. Available at: https://doi.org/10.1016/0013-4694(94)90112-0.

Nunez, P.L., Nunez, M.D. and Srinivasan, R. (2019) ‘Multi-scale neural sources of EEG: genuine, equivalent, and representative. A tutorial review’, *Brain Topography*, 32(2), pp. 193–214.

Oostenveld, R. *et al.* (2011) ‘FieldTrip: Open Source Software for Advanced Analysis of MEG, EEG, and Invasive Electrophysiological Data’, *Computational Intelligence and Neuroscience*, 2011, pp. 1–9. Available at: https://doi.org/10.1155/2011/156869.

Pascual-Marqui, R.D. *et al.* (2006) ‘Exact low resolution brain electromagnetic tomography (eLORETA)’, *Neuroimage*, 31(Suppl 1).

Pascual-Marqui, R.D., Michel, C.M. and Lehmann, D. (1994) ‘Low resolution electromagnetic tomography: a new method for localizing electrical activity in the brain’, *International Journal of Psychophysiology*, 18(1), pp. 49–65. Available at: https://doi.org/10.1016/0167-8760(84)90014-X.

Paz-Linares, D. *et al.* (2017) ‘Spatio temporal EEG source imaging with the hierarchical bayesian Elastic Net and Elitist Lasso models’, *Frontiers in Neuroscience*, 11(NOV). Available at: https://doi.org/10.3389/fnins.2017.00635.

Paz-Linares, D. *et al.* (2018) ‘Neural Connectivity with Hidden Gaussian Graphical State-Model’. Available at: http://arxiv.org/abs/1810.01174.

Paz-Linares, D. *et al.* (2023) ‘Minimizing the distortions in electrophysiological source imaging of cortical oscillatory activity via Spectral Structured Sparse Bayesian Learning’, *Frontiers in Neuroscience*, 17. Available at: https://doi.org/10.3389/fnins.2023.978527.

Piastra, M.C. *et al.* (2020) ‘A comprehensive study on electroencephalography and magnetoencephalography sensitivity to cortical and subcortical sources’, *Human Brain Mapping* [Preprint]. Available at: https://doi.org/10.1002/hbm.25272.

Piastra, M.C. *et al.* (2021) 'A comprehensive study on electroencephalography and magnetoencephalography sensitivity to cortical and subcortical sources', *Human Brain Mapping*, 42(4), pp. 978–992. Available at: https://doi.org/10.1002/hbm.25272.

Poplawsky, A.J., Fukuda, M. and Kim, S.-G. (2019) 'Foundations of layer-specific fMRI and investigations of neurophysiological activity in the laminarized neocortex and olfactory bulb of animal models', *NeuroImage*, 199, pp. 718–729. Available at: https://doi.org/10.1016/j.neuroimage.2017.05.023.

Reid, A.T. *et al.* (2019) 'Advancing functional connectivity research from association to causation', *Nature neuroscience*, 22(11), pp. 1751–1760.

Riaz, U. *et al.* (2020) 'Are Sources of EEG and MEG rhythmic activity the same? An analysis based on BC-VARETA', *bioRxiv*, p. 748996.

Riaz, U. *et al.* (2021) 'Stepwise Covariance-Free Common Principal Components (CF-CPC) With an Application to Neuroscience.', *Frontiers in neuroscience*, 15, p. 750290. Available at: https://doi.org/10.3389/fnins.2021.750290.

Riera, J.J. and Fuentes, M.E. (1998) 'Electric lead field for a piecewise homogeneous volume conductor model of the head', *IEEE Transactions on Biomedical Engineering*, 45(6), pp. 746–753. Available at: https://doi.org/10.1109/10.678609.

Schrader, S. *et al.* (2021) 'DUNEuro—A software toolbox for forward modeling in bioelectromagnetism', *PLOS ONE*, 16(6), pp. 1–21. Available at: https://doi.org/10.1371/journal.pone.0252431.

Sherif, T. *et al.* (2014) 'CBRAIN: a web-based, distributed computing platform for collaborative neuroimaging research', *Frontiers in Neuroinformatics*, 8. Available at: https://doi.org/10.3389/fninf.2014.00054.

Smith, S.M. *et al.* (2004) 'Advances in functional and structural MR image analysis and implementation as FSL', *NeuroImage*, 23, pp. S208–S219. Available at: https://doi.org/10.1016/j.neuroimage.2004.07.051.

Sotiropoulos, S.N. *et al.* (2013) 'Advances in diffusion MRI acquisition and processing in the Human Connectome Project', *NeuroImage*, 80, pp. 125–143. Available at: https://doi.org/10.1016/j.neuroimage.2013.05.057.

Strang, G., Fix, G.J. and Griffin, D.S. (1974) 'An analysis of the finite-element method'.

Symms, M. (2004) 'A review of structural magnetic resonance neuroimaging', *Journal of Neurology, Neurosurgery & Psychiatry*, 75(9), pp. 1235–1244. Available at: https://doi.org/10.1136/jnnp.2003.032714.

Tadel, F. *et al.* (2011) 'Brainstorm: A user-friendly application for MEG/EEG analysis', *Computational Intelligence and Neuroscience*, 2011. Available at: https://doi.org/10.1155/2011/879716.

Theaud, G. *et al.* (2020) 'TractoFlow: A robust, efficient and reproducible diffusion MRI pipeline leveraging Nextflow & Singularity', *NeuroImage*, 218, p. 116889. Available at: https://doi.org/10.1016/j.neuroimage.2020.116889.

Trujillo-Barreto, N.J., Aubert-Vázquez, E. and Valdés-Sosa, P.A. (2004) 'Bayesian model averaging in EEG/MEG imaging', *NeuroImage*, 21(4), pp. 1300–1319.

Uddin, L.Q. (2013) 'Complex relationships between structural and functional brain connectivity', *Trends in Cognitive Sciences*, 17(12), pp. 600–602. Available at: https://doi.org/10.1016/j.tics.2013.09.011.

Ulbert, I. *et al.* (2004) 'In vivo laminar electrophysiology co-registered with histology in the hippocampus of patients with temporal lobe epilepsy', *Experimental Neurology*, 187(2), pp. 310–318. Available at: https://doi.org/10.1016/j.expneurol.2003.12.003.

Valdes, P.A. *et al.* (1999) 'Nonlinear EEG analysis based on a neural mass model', *Biological Cybernetics*, 81(5–6), pp. 415–424. Available at: https://doi.org/10.1007/s004220050572.

Valdes-Sosa, P.A. *et al.* (2009) 'Model driven EEG/fMRI fusion of brain oscillations', *Human Brain Mapping*, 30(9), pp. 2701–2721. Available at: https://doi.org/10.1002/hbm.20704.

Valdes-Sosa, P.A. *et al.* (2021) 'The Cuban Human Brain Mapping Project, a young and middle age population-based EEG, MRI, and cognition dataset', *Scientific Data*, 8(1), p. 45. Available at: https://doi.org/10.1038/s41597-021-00829-7.

Van Essen, D.C. *et al.* (2013) 'The WU-Minn Human Connectome Project: An overview', *NeuroImage*, 80, pp. 62–79. Available at: https://doi.org/10.1016/j.neuroimage.2013.05.041.

Vassal, F. *et al.* (2016) 'Combined DTI Tractography and Functional MRI Study of the Language Connectome in Healthy Volunteers: Extensive Mapping of White Matter Fascicles and Cortical Activations', *PLOS ONE*. Edited by X.-N. Zuo, 11(3), p. e0152614. Available at: https://doi.org/10.1371/journal.pone.0152614.

Van Veen, B.D. *et al.* (1997) 'Localization of brain electrical activity via linearly constrained minimum variance spatial filtering', *IEEE Transactions on Biomedical Engineering*, 44(9), pp. 867–880. Available at: https://doi.org/10.1109/10.623056.

Vega, M.L.B. *et al.* (2021) 'Auto-QCLF: A Quick and Reliable EEG Lead Field Quality Control for Big Databases', *International Journal of Psychophysiology*, 168, pp. S183–S184.

Vinck, M. and Perrenoud, Q. (2019) 'Layers of Rhythms — from Cortical Anatomy to Dynamics', *Neuron*, 101(3), pp. 358–360. Available at: https://doi.org/10.1016/j.neuron.2019.01.028.

Vorwerk, J. *et al.* (2014) 'A guideline for head volume conductor modeling in EEG and MEG.', *NeuroImage*, 100, pp. 590–607. Available at: https://doi.org/10.1016/j.neuroimage.2014.06.040.

Vorwerk, J. *et al.* (2018) 'The FieldTrip-SimBio pipeline for EEG forward solutions', *Biomedical engineering online*, 17(1), pp. 1–17.

Wang, C., Yoldemir, B. and Abugharbieh, R. (2015) 'Multimodal Cortical Parcellation Based on Anatomical and Functional Brain Connectivity', in N. Navab et al. (eds) *Medical Image Computing and Computer-Assisted Intervention – MICCAI 2015*. Cham: Springer International Publishing, pp. 21–28.

Windhoff, M., Opitz, A. and Thielscher, A. (2013) 'Electric field calculations in brain stimulation based on finite elements: An optimized processing pipeline for the generation and usage of accurate individual head models', *Human Brain Mapping*, 34(4), pp. 923–935. Available at: https://doi.org/10.1002/hbm.21479.

Woolrich, M.W. *et al.* (2009) 'Bayesian analysis of neuroimaging data in FSL', *NeuroImage*, 45(1), pp. S173–S186. Available at: https://doi.org/10.1016/j.neuroimage.2008.10.055.

Xiao, Y. *et al.* (2019) 'An accurate registration of the BigBrain dataset with the MNI PD25 and ICBM152 atlases', *Scientific Data*, 6(1), p. 210. Available at: https://doi.org/10.1038/s41597-019-0217-0.

Yamaguchi, E. (2014) 'Finite element method', *Bridge Engineering Handbook: Fundamentals, Second Edition*, pp. 225–251. Available at: https://doi.org/10.1201/b15616.